Phase-locking of tearing modes in the reversed field experiment

Richard Fitzpatrick and Paolo Zanca

Phase-locking of tearing modes in the reversed field experiment

Richard Fitzpatrick[a)]
Institute for Fusion Studies, Department of Physics, University of Texas at Austin, Austin, Texas 78712

Paolo Zanca[b)]
Conzorzio RFX, Corso Stati Uniti 4, 35127 Padova, Italy

In the reversed field experiment (RFX) [F. Gnesotto *et al.*, Fusion Eng. Des. **25**, 335 (1995)], the $m=1$ and $m=0$ tearing modes present in the plasma are observed to phase-lock together to form a highly peaked, strongly toroidally localized, pattern in the perturbed magnetic field. This pattern, which is commonly known as the ''slinky'' pattern, gives rise to severe edge loading problems which limit the maximum achievable toroidal current. A theory is presented which explains virtually all salient features of the RFX slinky pattern. The central premise of this theory is that at high ambient mode amplitude the various tearing modes occurring in the plasma phase-lock together in a configuration which minimizes the magnitudes of the electromagnetic torques exerted at the various mode rational surfaces. The theory successfully predicts the profiles of the edge radial and toroidal magnetic fields generated by the $m=0$ and $m=1$ modes, the phase relations between the various modes, the presence of a small toroidal offset between the peaks of the $m=0$ and $m=1$ contributions to the overall slinky pattern, and the response of the pattern to externally generated $m=0$ and $m=1$ magnetic perturbations. © *2002 American Institute of Physics.*
[DOI: 10.1063/1.1481057]

I. INTRODUCTION

A reversed field pinch (RFP) is a toroidal magnetic configuration for thermonuclear plasma confinement characterized by a short and rapidly varying helical pitch of the magnetic field. The cylindrical safety factor,[1] q, monotonically decreases from a typical value of $q \simeq (\frac{1}{2}) \, a/R_0$ on the toroidal magnetic axis to $q \simeq -(\frac{1}{6}) \, (a/R_0)$ at the edge of the plasma, passing through zero at $r/a \simeq 0.8$ (a and R_0 are the minor and major radii, respectively, of the plasma torus). As is well-known, a configuration in which the edge toroidal magnetic field (and, hence, the edge-q) is reversed is maximally stable to magnetohydrodynamical (MHD) modes.[2] A conventional RFP is surrounded by a close fitting, highly conducting shell which stabilizes external-kink modes which would otherwise rapidly destroy the plasma. The remaining instabilities are internally resonant modes (i.e., they satisfy $k \cdot B = 0$ somewhere inside the plasma, where k is the wave vector and B the equilibrium magnetic field) which tear and reconnect the magnetic field at their associated resonant surfaces. These instabilities, which are known as *tearing modes*, play a double role in RFP physics. Firstly, tearing mode activity converts the magnetic flux generated by the poloidal field transformer into toroidal flux; thus, maintaining the reversal of the edge toroidal magnetic field, which would otherwise rapidly decay away.[3] Secondly, tearing modes reconnect magnetic-field lines to generate overlapping chains of magnetic islands. These overlapping island chains ergodize the magnetic field; thereby, strongly degrading the plasma energy confinement.[4]

A tearing mode is conveniently identified via its poloidal mode number, m (i.e., the number of periods the short way around the plasma torus), and its toroidal mode number, n (i.e., the number of periods the long way around the plasma torus). The m, n mode is resonant inside the plasma where $q = m/n$. The dominant tearing modes in conventional RFP plasmas are $m=1$ modes, resonant in the plasma core, and $m=0$ modes, resonant at the *reversal surface* (i.e., the surface on which the equilibrium toroidal magnetic field passes through zero), which is situated close to the plasma edge. The number of unstable $m=1$ and $m=0$ modes is largely controlled by the inverse aspect-ratio, $\epsilon_a = a/R_0$, of the plasma torus. The smaller ϵ_a, the larger the number of unstable modes. For a typical present-day RFP, such as RFX (the Reversed Field eXperiment[5]), for which $\epsilon_a = 0.23$, the dominant $m=1$ modes have toroidal mode numbers lying in the range $n = 7-15$, whereas the dominant $m=0$ modes have toroidal mode numbers lying in the range $n = 1-15$.

In virtually all RFP experiments, the $m=1$ and $m=0$ tearing modes present in the plasma are observed to *phase-lock* together to form a highly peaked, strongly toroidally localized, pattern in the perturbed magnetic field, which is sometimes called the *slinky pattern*.[6–10] The slinky pattern gives rise to a toroidally localized distortion of the plasma torus which causes its outermost flux-surfaces to intersect the wall; thereby, generating a localized wall ''hot spot.'' [11] If the slinky pattern locks to the wall (as is always the case in RFX) then this hot spot can easily cause wall overheating, leading to the influx of impurities into the plasma, and the eventual termination of the discharge. Indeed, the maximum achievable plasma current in RFX is strongly limited by this effect. Fortunately, however, the overheating problems asso-

ciated with the hot spot can be partially alleviated by forcing the slinky pattern to rotate.[12,13]

Wall locking of the slinky pattern is presumably caused by the phase-locking of its constituent tearing modes to static error-fields. For RFPs which possesses a thin, resistive vacuum vessel located inside the stabilizing shell (e.g., RFX), the locking of tearing modes to static error-fields is greatly facilitated by vacuum vessel eddy currents.[14,15]

The aim of our paper is to gain a theoretical understanding of how and why phase-locking occurs in RFX plasmas. Rather than attempting a three-dimensional, nonlinear-MHD simulation of phase-locking,[16,17] we shall build on the previously published analytical results of Fitzpatrick,[18] and the detailed observations of the phase relations between phase-locked modes in RFX, which were recently obtained by Zanca et al.[19] Our analysis is restricted to zero-β, resistive, viscous, MHD.

This paper is organized as follows. After some preliminary analysis in Sec. II, we outline our theory of $m=0$ and $m=1$ phase-locking in Secs. III and IV, respectively. Section V discusses phase-locking to error-fields. In Sec. VI, we compare our theory with experimental data from RFX. We present some simulations of RFX discharges in Sec. VII. Finally, in Sec. VIII, we summarize and discuss our results.

II. PRELIMINARY ANALYSIS

A. Plasma equilibrium

Consider a large aspect-ratio,[20] zero-β,[21] axisymmetric, toroidal plasma equilibrium whose unperturbed magnetic flux-surfaces map out (almost) concentric circles in the poloidal plane. Such an equilibrium is well approximated as a periodic cylinder. Suppose that the minor radius of the plasma is a. Standard right-handed, cylindrical polar coordinates (r, θ, z) are adopted. The system is assumed to be periodic in the z direction, with periodicity length $2\pi R_0$, where R_0 is the simulated plasma major radius. It is convenient to define a simulated toroidal angle $\phi = z/R_0$. The equilibrium magnetic field is written $\boldsymbol{B} = [0, B_\theta(r), B_\phi(r)]$, where $\nabla \wedge \boldsymbol{B} = \sigma(r)\boldsymbol{B}$.

B. Perturbed magnetic field

The magnetic perturbation associated with an m, n tearing mode can be written $\boldsymbol{b}(\boldsymbol{r},t) = \boldsymbol{b}^{m,n}(r,t)e^{i(m\theta - n\phi)}$. In this paper, it is assumed that $m \geq 0$ and $n > 0$. The components of the perturbed magnetic field are written[18]

$$b_r^{m,n} = i\frac{\psi^{m,n}}{r}, \tag{1}$$

$$b_\theta^{m,n} = -\frac{m(d\psi^{m,n}/dr)}{m^2 + n^2\epsilon^2} + \frac{n\epsilon\sigma\psi^{m,n}}{m^2 + n^2\epsilon^2}, \tag{2}$$

$$b_\phi^{m,n} = \frac{n\epsilon(d\psi^{m,n}/dr)}{m^2 + n^2\epsilon^2} + \frac{m\sigma\psi^{m,n}}{m^2 + n^2\epsilon^2}, \tag{3}$$

where $\epsilon = r/R_0$. The linearized magnetic flux-function $\psi^{m,n}(r,t)$ satisfies Newcomb's equation.[22,23] As is well-known, Newcomb's equation is *singular* at the m/n resonant (or "rational") surface, minor radius $r_s^{m,n}$, which satisfies

$F^{m,n}(r_s^{m,n}) = 0$ [i.e., $q(r_s^{m,n}) = m/n$], where $F^{m,n}(r) \equiv mB_\theta - n\epsilon B_\phi$. This singularity is resolved by the presence of a magnetic island chain centerd on the rational surface.

Let $\hat{\psi}^{m,n}(r)$ represent the normalized m, n tearing eigenfunction. In other words, $\hat{\psi}^{m,n}(r)$ is a *real*, continuous solution to Newcomb's equation which is well behaved as $r \to 0$, satisfies $\hat{\psi}^{m,n}(r_s^{m,n}) = 1$, and satisfies $\hat{\psi}^{m,n}(c) = 0$. Here, $r = c$ is the minor radius of the highly conducting shell surrounding the plasma. The above prescription uniquely specifies $\hat{\psi}^{m,n}(r)$. In general, $\hat{\psi}^{m,n}(r)$ possesses a gradient discontinuity at $r = r_s^{m,n}$. The real quantity

$$E^{m,n} = \left[r\frac{d\hat{\psi}^{m,n}}{dr}\right]_{r_s^{m,n}-}^{r_s^{m,n}+}, \tag{4}$$

can be identified as the standard *linear stability index* for the m, n tearing mode.[24] In this paper, it is assumed that the dominant tearing modes in a given RFP plasma are those for which $E^{m,n} > 0$.

We can write

$$\psi^{m,n}(r,t) = \hat{\psi}^{m,n}(r)\Psi^{m,n}(t)e^{i\varphi^{m,n}(t)}, \tag{5}$$

where $\Psi^{m,n}(t)$ and $\varphi^{m,n}(t)$ are the amplitude and phase of the m, n mode, respectively. In the following, we concentrate on the time evolution of the $\varphi^{m,n}(t)$. The mode amplitudes are regarded as fixed quantities to be derived from observations.

C. Error-field

In this paper, we assume that any externally generated error-field leaks through narrow gaps in the highly conducting shell. Inside the shell, the vacuum magnetic perturbation associated with a general error-field is written

$$\boldsymbol{b}_{vac} = \sum_{m,n} \mathcal{C}^{m,n}\nabla\psi_{vac}^{m,n}(r,\theta,\phi,t)\wedge\boldsymbol{n}^{m,n}, \tag{6}$$

where $\mathcal{C}^{m,n} = (m^2 + n^2\epsilon^2)^{-1/2}$ and $\boldsymbol{n}^{m,n} = \mathcal{C}^{m,n}(0,n\epsilon,m)$. Let

$$\psi_{vac}^{m,n}(c,\theta,\phi,t) = \Psi_v^{m,n}(t)e^{i\varphi_v^{m,n}(t)}e^{i(m\theta - n\theta)}, \tag{7}$$

where $\Psi_v^{m,n}$ and $\varphi_v^{m,n}$ are the amplitude and phase of the m, n component of the error-field, respectively, just inside the shell.

III. PHASE-LOCKING OF M=0 MODES

A. Introduction

In this section, we shall investigate the mutual phase-locking of the $m=0$ modes. For the moment, we shall ignore the $m=1$ modes. According to conventional MHD theory, the phase of a tearing mode is entirely determined by plasma motion in the immediate vicinity of its rational surface.[25] Of course, the $m=0$ modes all share the same rational surface: i.e., the reversal surface, radius r_*, which satisfies $B_\phi(r_*) = 0$. Thus, it should be possible to formulate a theory of $m=0$ phase-locking by concentrating on plasma dynamics at the reversal surface.

In the following, we present two complementary theories of $m=0$ phase-locking. The first theory uses a variational approach, whereas the second employs a Fourier approach.

B. Variational analysis

The radial component of the curl of the linearized MHD Ohm's law yields

$$-\frac{\partial b_r}{\partial t}+\frac{B_\phi}{R_0}\frac{\partial v_r}{\partial \phi}=-\frac{\eta}{R_0}\frac{\partial j_\theta}{\partial \phi}, \tag{8}$$

in the instantaneous rest frame of the plasma at the reversal surface. Here, $b_r(r,\phi,t)$, $v_r(r,\phi,t)$, and $j_\theta(r,\phi,t)$ are the radial magnetic-field perturbation, radial plasma velocity perturbation, and poloidal current perturbation, respectively, associated with the $m=0$ modes. Furthermore, $\eta(r)$ is the plasma resistivity.

Throughout the bulk of the plasma, the two terms on the left-hand side of the above equation balance one another, and the term on the right-hand side is negligible. This ordering enforces the familiar ideal-MHD flux-freezing constraint. However, flux-freezing breaks down in the immediate vicinity of the reversal surface, where $B_\phi \simeq 0$. In this nonideal region, the term on the right-hand side of Eq. (8) becomes important. In other words, a (radially) thin poloidal current sheet flows in the vicinity of the reversal surface.

We can radially integrate Eq. (8) over the nonideal region in the vicinity of the reversal surface to give

$$-\delta\frac{\partial b_*}{\partial t}\approx-\frac{\eta_*}{R_0}\frac{\partial J_*}{\partial \phi}. \tag{9}$$

Here, δ is the radial thickness of the nonideal region, $\eta_* = \eta(r_*)$, $b_*(\phi,t)=b_r(r_*,\phi,t)$, and $J_*(\phi,t) = \int_{r_*^-}^{r_*^+} j_\theta(r,\phi,t)dr$. In writing the above expression, we have assumed that b_r is approximately constant over the nonideal region (which corresponds to the familiar constant-ψ approximation[24]), and have neglected the term involving v_r. It is convenient to write

$$b_*(\phi,t)=\hat{b}_*(\phi)e^{\gamma t}, \tag{10}$$

$$J_*(\phi,t)=\hat{J}_*(\phi)e^{\gamma t}, \tag{11}$$

in which case Eq. (9) reduces to

$$\hat{b}_*(\phi)\simeq\frac{\eta_*}{\gamma\delta R_0}\frac{d\hat{J}_*}{d\phi}. \tag{12}$$

Note that the simplifying assumption of a common time dependence of the $m=0$ modes is fairly consistent with experimental observations (see Sec. VI). The radially integrated toroidal electromagnetic torque acting in the vicinity of the reversal surface can be written $T_*(\phi,t) = \hat{T}_*(\phi)e^{2\gamma t}$, where

$$\hat{T}_*(\phi)=-R_0\hat{J}_*\hat{b}_*\simeq-\frac{\eta_*}{2\gamma\delta}\frac{d(\hat{J}_*^2)}{d\phi}. \tag{13}$$

The above electromagnetic torque must be balanced by plasma inertia and viscosity. However, the amplitude of the

electromagnetic torque increases as the square of the ambient $m=0$ mode amplitude, whereas plasma inertia and viscosity remain approximately the same. It follows that torque balance becomes quite problematic in the high mode amplitude regime. Our hypothesis is that when the ambient mode amplitude becomes sufficiently high the $m=0$ modes phase-lock together in such a manner as to *minimize* the magnitude of the electromagnetic torque—thereby, facilitating torque balance. This hypothesis suggests that we minimize the magnitude of the torque, $\oint \hat{T}_*^2 d\phi$, for a fixed magnitude of the current sheet, $\oint \hat{J}_*^2 d\phi$. In other words, we seek a $\hat{J}_*(\phi)$ profile which minimizes the functional

$$W[\hat{J}_*]=\oint\left[\frac{d(\hat{J}_*^2)}{d\phi}\right]^2 d\phi+\lambda\oint\hat{J}_*^2 d\phi, \tag{14}$$

where λ is a Lagrange multiplier. Standard variational analysis yields

$$\frac{d^2(\hat{J}_*^2)}{d\phi^2}=\frac{\lambda}{2}, \tag{15}$$

or

$$\hat{J}_*^2=\frac{\lambda\phi^2}{4}+\alpha\phi+\beta, \tag{16}$$

where α and β are constants of integration.

Now, the current profile $\hat{J}_*(\phi)$ must satisfy a couple of constraints. Firstly,

$$\oint\hat{J}_*d\phi=0, \tag{17}$$

since the $m=0$ modes cannot self-generate a net poloidal current at the reversal surface. Secondly, $\hat{J}_*(\phi)$ must be periodic in ϕ, with period 2π. The above constraints can only be satisfied (for physical $\hat{J}_*$ profiles) if the right-hand side of Eq. (16) is a perfect square. In fact, we can write

$$\hat{J}_*(\phi)=\frac{J_0}{\pi}(\phi-\phi_0-\pi), \tag{18}$$

for $0<\phi-\phi_0<2\pi$, where J_0 can either be positive or negative. Note that $\hat{J}_*$ must be discontinuous whenever $\phi-\phi_0$ is an integer multiple of 2π, in order to maintain periodicity. Nevertheless, $\hat{J}_*^2$ is continuous, and the integral $\oint[d(\hat{J}_*^2)/d\phi]^2 d\phi$ possesses no singularities. It follows from Eq. (12) that

$$\hat{b}_*(\phi)=\frac{2J_0\eta_*}{\gamma\delta R_0}\left[\frac{1}{2\pi}-\delta(\phi-\phi_0)\right], \tag{19}$$

for $0\leq\phi-\phi_0\leq2\pi$. The optimal $\hat{J}_*$ and $\hat{b}_*$ profiles are sketched in Fig. 1 for positive J_0. Of course, for negative J_0 the profiles are inverted.

Note that a variational calculation can only be made for the $m=0$ perturbation, because only at the reversal surface is there a broad spectrum of unstable resonant modes. Hence, only at the reversal surface can we talk about a *variable*
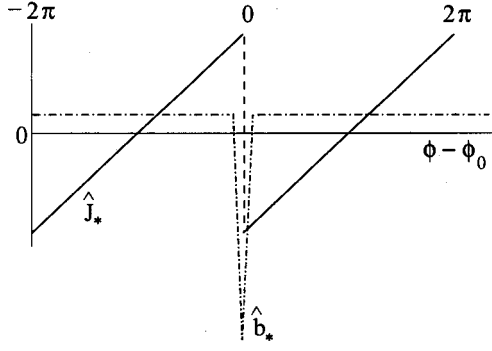
FIG. 1. Sketch of the $\hat{J}_*$ and $\hat{b}_*$ profiles which minimize the amplitude of the $m=0$ generated electromagnetic torque at the reversal surface.

angular profile of the perturbation. Clearly, relations similar to Eqs. (9)–(13) can also be written at the 1, n rational surfaces; however, at these surfaces the angular profiles of the poloidal and toroidal current sheets are *fixed*, because there is only a single unstable resonant mode.

C. Fourier analysis

Ampère's law yields

$$\mu_0 J_* = -[b_\phi]_{r_*-}^{r_*+}, \tag{20}$$

where $b_\phi(r,\phi,t)$ is the toroidal magnetic field perturbation due to the $m=0$ modes. It is easily demonstrated that

$$[b_\phi^{0,n}]_{r_*-}^{r_*+} = \frac{E^{0,n}\Psi^{0,n}}{n\epsilon_* r_*}\cos(n\phi - \varphi^{0,n}), \tag{21}$$

with $\epsilon_* = r_*/R_0$. Hence,

$$J_*(\phi) = -\frac{1}{\mu_0\epsilon_* r_*}\sum_{n>0}\frac{E^{0,n}\Psi^{0,n}}{n}\cos(n\phi - \varphi^{0,n}), \tag{22}$$

where the sum is taken over the dominant $m=0$ modes: i.e., those modes for which $E^{0,n}>0$. It is also easily demonstrated that

$$b_*(\phi) = \frac{1}{r_*}\sum_{n>0}\Psi^{0,n}\sin(n\phi - \varphi^{0,n}). \tag{23}$$

Finally, the radially integrated toroidal torque acting in the vicinity of the reversal surface takes the form

$$T_*(\phi) = -R_0 J_* b_*. \tag{24}$$

As before, we hypothesize that when the ambient mode amplitude becomes sufficiently large the various $m=0$ modes phase-lock together in such a manner as to minimize the magnitude of the electromagnetic torque at the reversal surface. Now, phase-locking of the $m=0$ modes implies that $\varphi^{0,n+1}-\varphi^{0,n}$ is the same for all the locked modes. In other words

$$\varphi^{0,n} = n\phi_0 - \Delta_0, \tag{25}$$

where Δ_0 is, as yet, undetermined. Equations (22)–(25) yield

$$T_* = \frac{1}{2\mu_0\epsilon_*^2 r_*}$$

$$\times\sum_{j>0}\{C_j\cos[j(\phi - \phi_0)] + S_j\sin[j(\phi - \phi_0)]\}, \tag{26}$$

where

$$C_j = \sum_{n>0}\frac{E^{0,n}\Psi^{0,n}\Psi^{0,j-n}}{n}\sin(2\Delta_0), \tag{27}$$

$$S_j = \sum_{n>0}\frac{E^{0,n}\Psi^{0,n}}{n}$$

$$\times[\Psi^{0,j-n}\cos(2\Delta_0) + \Psi^{0,n+j} - \Psi^{0,n-j}]. \tag{28}$$

We wish to minimize $\oint T_*^2 d\phi$ with respect to Δ_0 in order to find the phase-locked $m=0$ configuration which minimizes the magnitude of the electromagnetic torque. It is easily demonstrated that

$$\frac{1}{2\pi}\oint T_*^2 d\phi = T_0 + T_2\cos(2\Delta_0), \tag{29}$$

where

$$T_2 = \frac{1}{(2\mu_0\epsilon_*^2 r_*)^2}\sum_{j>1}a_j b_j, \tag{30}$$

and

$$a_j = \sum_{n>0}\frac{E^{0,n}\Psi^{0,n}\Psi^{0,j-n}}{n}, \tag{31}$$

$$b_j = \sum_{n>0}\Psi^{0,n}\Psi^{0,n+j}\left(\frac{E^{0,n}}{n} - \frac{E^{0,n+j}}{n+j}\right). \tag{32}$$

It follows that the optimum values of Δ_0 are $\pm\pi/2$ if $T_2 > 0$ and $0, \pi$ if $T_2 < 0$.

Recall that the dominant $m=0$ modes are those which are tearing unstable: i.e., those for which $E^{0,n}>0$. Moreover, the $m=0$ mode amplitudes, $\Psi^{0,n}$, and toroidal mode numbers, n, are positive definite. Finally, for all plausible equilibrium current profiles, $E^{0,n}$ decreases as n increases—see Table I. Hence, it follows that the a_j and the b_j are all positive, which implies that $T_2 > 0$. We conclude that the optimum phase-locked configuration for the $m=0$ modes is characterized by $\Delta_0 = \pm\pi/2$. It follows from Eqs. (22), (23), and (25) that

$$J_*(\phi) = \frac{\mathrm{sgn}(\Delta_0)}{\mu_0\epsilon_* r_*}\sum_{n>0}\frac{E^{0,n}\Psi^{0,n}}{n}\sin[n(\phi - \phi_0)], \tag{33}$$

$$b_*(\phi) = \frac{\mathrm{sgn}(\Delta_0)}{r_*}\sum_{n>0}\Psi^{0,n}\cos[n(\phi - \phi_0)]. \tag{34}$$

Suppose, for the sake of illustration, that the dominant $m=0$ modes possess toroidal mode numbers in the range 1 to N. Suppose, further, that the amplitudes, $\Psi^{0,n}$, and stability indices, $E^{0,n}$, of these modes are all the same. The latter assumptions are fairly realistic (experimental $m=0$ amplitudes do not usually exhibit a strong variation with n, and theoretical $E^{0,n}$ values generally vary weakly with n—see

TABLE I. The poloidal and toroidal mode numbers, rational surface radii, stability indices, and normalized edge radial and toroidal magnetic fields for the modes included in the phase-locking simulation of RFX shot 8071.

m	n	$r_s^{m,n}/a$	$E^{m,n}$	$\hat{b}_r^{m,n}$	$\hat{b}_\phi^{m,n}$
1	8	2.215e−1	4.992e+0	2.422e+0	−5.948e+0
1	9	3.507e−1	2.675e+0	1.182e+0	−2.717e+0
1	10	4.260e−1	1.977e+0	9.548e−1	−2.060e+0
1	11	4.784e−1	1.478e+0	8.500e−1	−1.727e+0
1	12	5.176e−1	1.043e+0	7.846e−1	−1.506e+0
1	13	5.484e−1	6.364e−1	7.363e−1	−1.340e+0
1	14	5.735e−1	2.411e−1	6.970e−1	−1.208e+0
0	1	8.441e−1	1.674e+1	1.970e+0	−4.647e+1
0	2	8.441e−1	1.662e+1	1.962e+0	−2.318e+1
0	3	8.441e−1	1.642e+1	1.949e+0	−1.539e+1
0	4	8.441e−1	1.616e+1	1.930e+0	−1.149e+1
0	5	8.441e−1	1.582e+1	1.907e+0	−9.115e+0
0	6	8.441e−1	1.541e+1	1.880e+0	−7.530e+0

Table I), and is also in accordance with the analysis of Sec. III B, where it was assumed that the dominant $m=0$ modes possessed a common time dependence. It follows that $J_* \propto \mathrm{sgn}(\Delta_0)\Sigma_{n=1,N} \sin[n(\phi-\phi_0)]/n$ and $b_* \propto \mathrm{sgn}(\Delta_0)\Sigma_{n=1,N} \times \cos[n(\phi-\phi_0)]$. Figure 2 shows the J_* and b_* profiles calculated, in this manner, for $N=15$. (We have selected $\Delta_0 <0$.) It can be seen that the profiles correspond almost perfectly to those sketched in Fig. 1. Indeed, the correspondence becomes exact in the limit $N\to\infty$.

D. Summary

Our main hypothesis is that when the ambient mode amplitude becomes sufficiently high the $m=0$ modes phase-lock together in a configuration which minimizes the magnitude of the electromagnetic torque exerted at the reversal surface. The analysis of Secs. III B and III C demonstrates that the phase-locked configuration is characterized by

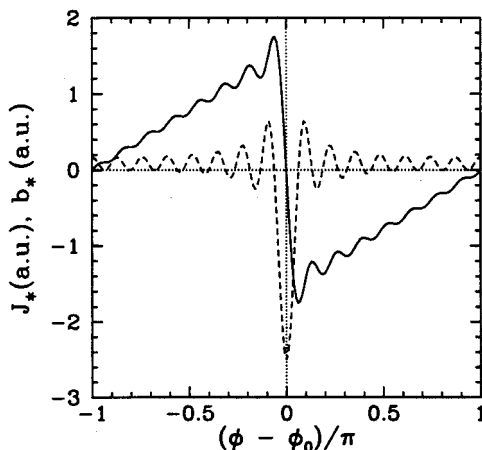$$\varphi^{0,n}=n\phi_0-\Delta_0, \qquad (35)$$

FIG. 2. The J_* (solid line) and b_* (dashed line) profiles which minimize the amplitude of the $m=0$ generated electromagnetic torque at the reversal surface, calculated for $N=15$.

where $\Delta_0=\pm\pi/2$. The above distribution of phases generates an $m=0$ radial field which has a "spike" at $\phi=\phi_0$ (the spike is positive or negative depending on whether $\Delta_0>0$ or $\Delta_0<0$)—see Figs. 1 and 2. The current sheet at the reversal surface generates an $m=0$ toroidal field outside the reversal surface which varies *linearly* with ϕ, and possesses a quasi-discontinuity at $\phi=\phi_0$ [the gradient of the field (w.r.t. ϕ) is positive or negative depending on whether $\Delta_0<0$ or $\Delta_0>0$]—in fact, the expected b_ϕ profile outside the reversal surface is similar to the J_* profile shown in Figs. 1 and 2 [this can be ascertained from Eq. (88), given that the $\hat{b}_\phi^{0,k}$ are all negative—see Table I]. The narrowness and height of the spike in b_r, and the steepness of the quasi-discontinuity in b_ϕ, all increase as the number of phase-locked $m=0$ modes increases.

IV. PHASE-LOCKING OF M=1 MODES

A. Introduction

Let us now consider the phase-locking of the $m=1$ modes. As discussed in Ref. 18, $m=1$ phase-locking is mediated by three-wave coupling involving triplets of two $m=1$ modes and a single $m=0$ mode.[26,27] Moreover, the strength of this coupling can be calculated using linear tearing eigenfunctions. Three-wave coupling leads to the development of net electromagnetic torques at the $m=1$ rational surfaces and the reversal surface.

B. Analysis

The flux-surface averaged, radially integrated, toroidal electromagnetic torque exerted at the reversal surface due to three-wave coupling between the 1, $n+k$ mode, the 1, n mode, and the 0, k mode is written[18]

$$T^{n,k}=-\frac{\pi^2 R_0}{2\mu_0}(\Psi^{1,n+k}\Psi^{1,n}\Psi^{0,k})\left(\mathcal{P}\int_0^a t_{n,k}(r)dr\right)$$
$$\times k\sin(\varphi^{1,n+k}-\varphi^{1,n}-\varphi^{0,k}), \qquad (36)$$

where $\mathcal{P}$ denotes a Cauchy principal part. Here, $\mathcal{P}\int_0^a t_{n,k}(r)dr$ is the so-called "overlap integral," whose integrand takes the form

$$t_{n,k}(r) = \frac{d\sigma}{dr}\left\{ r\frac{d\hat{\psi}^{1,n}}{dr}\hat{\psi}^{0,k}\hat{\psi}^{1,n+k}\frac{G^{1,n}}{H^{1,n}F^{0,k}F^{1,n+k}} \right.$$

$$+\hat{\psi}^{1,n}r\frac{d\hat{\psi}^{0,k}}{dr}\hat{\psi}_{1,n+k}\frac{G^{0,k}}{H^{0,k}F^{1,n}F^{1,n+k}}$$

$$+\hat{\psi}^{1,n}\hat{\psi}^{0,k}r\frac{d\hat{\psi}^{1,n+k}}{dr}\frac{G^{1,n+k}}{H^{1,n+k}F^{1,n}F^{0,k}}$$

$$+\hat{\psi}^{1,n}\hat{\psi}^{0,k}\hat{\psi}^{1,n+k}\left[r\sigma\left(\frac{F^{1,n}}{H^{1,n}F^{0,k}F^{1,n+k}} \right. \right.$$

$$\left. +\frac{F^{0,k}}{H^{0,k}F^{1,n}F^{1,n+k}}+\frac{F^{1,n+k}}{H^{1,n+k}F^{1,n}F^{0,k}} \right)$$

$$\left. \left. +\frac{2B_\theta B_\phi - r\sigma(B_\theta^2 + B_\phi^2)}{F^{1,n}F^{0,k}F^{1,n+k}} \right]\right\}, \tag{37}$$

where

$$F^{m,n}(r) = mB_\theta - n\epsilon B_\phi, \tag{38}$$

$$G^{m,n}(r) = n\epsilon B_\theta + mB_\phi, \tag{39}$$

$$H^{m,n}(r) = m^2 + n^2\epsilon^2. \tag{40}$$

Thus, the total torque at the reversal surface due to three-wave coupling is

$$T = \sum_{n,k} T^{n,k}, \tag{41}$$

where the sum is taken over the dominant $m=1$ and $m=0$ modes.

As before, we hypothesize that when the ambient mode amplitude becomes sufficiently high the $m=1$ modes phase-lock together in a configuration such that the absolute value of the electromagnetic torque exerted at the reversal surface due to three-wave coupling is minimized, since this is the only way in which such a torque could be balanced by plasma viscosity and inertia. (Note that minimization of the electromagnetic torque at the reversal surface also implies minimization of the electromagnetic torques at the $m=1$ rational surfaces, since zero net electromagnetic torque is exerted on the plasma, as a whole, as a consequence of three-wave coupling.) Now, phase-locking of the $m=1$ modes implies

$$\varphi^{1,n} = n\phi_1 - \Delta_1, \tag{42}$$

where Δ_1 is undetermined. Hence, Eqs. (35), (36), (41), and (42) yield

$$T(\phi_0 - \phi_1) = -\operatorname{sgn}(\Delta_0)\sum_{n,k}\frac{\pi^2 R_0}{2\mu_0}(\Psi^{1,n+k}\Psi^{1,n}\Psi^{0,k})$$

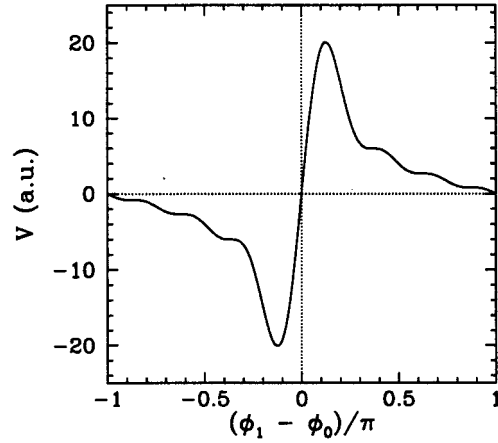$$\times\left(\mathcal{P}\int_0^a t_{n,k}(r)dr \right)k\cos[k(\phi_0 - \phi_1)]. \tag{43}$$

FIG. 3. The $m=1$ "locking potential" calculated for $N=8$.

It is convenient to express $T(\phi_0 - \phi_1)$ as the gradient of a potential:

$$V(\phi_0 - \phi_1) = -\int_0^{\phi_0-\phi_1} T(\varphi)d\varphi. \tag{44}$$

It follows that:

$$V(\phi_0 - \phi_1) = \operatorname{sgn}(\Delta_0)\sum_{n,k}\frac{\pi^2 R_0}{2\mu_0}(\Psi^{1,n+k}\Psi^{1,n}\Psi^{0,k})$$

$$\times\left(\mathcal{P}\int_0^a t_{n,k}(r)dr \right)\sin[k(\phi_0 - \phi_1)]. \tag{45}$$

Finding the minimum absolute value of the electromagnetic torque is equivalent to finding the minimum of the above potential. (The maximum of the potential would also minimize the absolute value of the torque, but is dynamically unstable.)

Suppose, for the sake of illustration, that the dominant $m=1$ modes possess toroidal mode numbers in the range n_1 to $n_1 + N - 1$, and the dominant $m=0$ modes possess toroidal mode numbers in the range 1 to N' (where $N' > N - 1$). Suppose, further, that the amplitudes of all the coupled modes are the same, and that all the overlap integrals are equal. The latter assumptions are fairly realistic. We obtain

$$V(\phi_1 - \phi_0) = -V(\phi_0 - \phi_1) \propto -\operatorname{sgn}(\Delta_0)$$

$$\times\sum_{k=1}^{N-1}(N-k)\sin[k(\phi_1 - \phi_0)]. \tag{46}$$

Here, we have tacitly assumed that the overlap integrals are positive. Figure 3 shows the "locking potential" calculated, in this manner, for $N=8$. (We have selected $\Delta_0 < 0$.) It can be seen that the potential possesses a strong minimum for ϕ_1 slightly less than ϕ_0. Hence, we conclude that the $m=1$ modes phase-lock in a configuration such that ϕ_0 slightly exceeds ϕ_1. (Selection of $\Delta_0 > 0$, or negative overlap integrals, would lead to the opposite conclusion.)

The radial field perturbation associated with the $m=1$ modes can be written
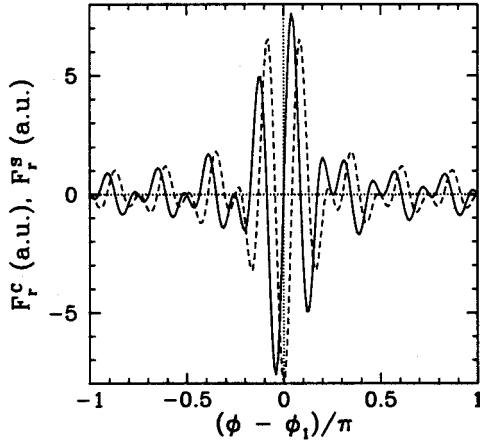
FIG. 4. The cosine and sine "envelope functions," F_r^C (solid line) and F_r^S (dashed line), for the $m=1$ radial field, calculated for $n_1=8$ and $N=8$.

$$b_r(\theta,\phi) \propto \cos(\theta - \Delta_1) F_r^C(\phi - \phi_1)$$
$$+ \sin(\theta - \Delta) F_r^S(\phi - \phi_1), \qquad (47)$$

where

$$F_r^C(\phi - \phi_1) = \sum_{n=n_1}^{n_1+N-1} \sin[n(\phi - \phi_1)], \qquad (48)$$

$$F_r^S(\phi - \phi_1) = -\sum_{n=n_1}^{n_1+N-1} \cos[n(\phi - \phi_1)]. \qquad (49)$$

Figure 4 shows the cosine and sine "envelope functions," F_r^C and F_r^S, for the $m=1$ radial field, calculated for $n_1=8$ and $N=8$. It can be seen that the envelope functions are highly peaked and strongly toroidally localized around $\phi = \phi_1$.

C. Summary

Our central hypothesis—that when the ambient mode amplitude becomes sufficiently high the $m=0$ and $m=1$ modes phase-lock together in a configuration which minimizes the magnitude of the electromagnetic torque exerted at the reversal surface—allows us to make detailed predictions regarding the form of the phase-locked configuration. The $m=1$ modes phase-lock in a configuration which is highly peaked and strongly toroidally localized about some toroidal angle $\phi = \phi_1$. There are two, equally probable, phase-locked configurations for the $m=0$ modes—corresponding to the choice $\Delta_0 = \pm \pi/2$. For the choice of the upper sign, the $m=0$ radial field possesses a strong *positive* "spike" at toroidal angle $\phi = \phi_0$, whereas the edge $m=0$ toroidal field *decreases* linearly with ϕ, and possesses a quasi-discontinuity at $\phi = \phi_0$. For the choice of the lower sign, the $m=0$ radial field possesses a strong *negative* spike at toroidal angle $\phi = \phi_0$, whereas the edge $m=0$ toroidal field *increases* linearly with ϕ, and possesses a quasi-discontinuity at $\phi = \phi_0$. There is a slight offset between the angles ϕ_1 and ϕ_0. For the choice of the upper sign, ϕ_1 slightly *exceeds* ϕ_0, and *vice versa* for the choice of the lower sign. (Here, we are assuming that the overlap integrals are positive—if the inte-

grals are negative then the offset reverses sign.) The strength of the peaking and toroidal localization of the net $m=0$ and $m=1$ magnetic perturbations increases as the number of phase-locked modes increases. Finally, the magnitude of the offset between ϕ_0 and ϕ_1 decreases as the number of phase-locked modes increases.

V. PHASE-LOCKING TO ERROR-FIELDS

A. Introduction

RFP plasmas invariably rotate in the laboratory frame. Thus, in general, we would expect the slinky pattern to also rotate as its constituent tearing modes are convected by the plasma. However, in the RFX experiment, the rotation of the slinky pattern is arrested via the phase-locking of some of its constituent tearing modes to static error-fields. Let us investigate this effect.

B. Phase-locking to an $m=0$ error-field

Consider the effect of a 0, 1 error-field of amplitude $\Psi_v^{0,1}$ and phase $\varphi_v^{0,1}$. The additional flux-surface averaged, radially integrated, toroidal torque generated at the reversal surface is written[18]

$$T_*' = -\frac{2\pi^2 R_0}{\mu_0 \epsilon_*^2} E_{sc}^{0,1} \Psi_v^{0,1} \Psi^{0,1} \sin(\varphi^{0,1} - \varphi_v^{0,1}), \qquad (50)$$

where

$$E_{sc}^{m,n} = \frac{\hat{\psi}^{m,n}(a)(m^2 + n^2 \epsilon_s^2)}{k_m(n\epsilon_c) i_m(n\epsilon_a) - k_m(n\epsilon_a) i_m(n\epsilon_c)}, \qquad (51)$$

with $\epsilon_a = a/R_0$, $\epsilon_c = c/R_0$, and $\epsilon_s = r_s^{m,n}/R_0$. Here, $k_m()$ and $i_m()$ are vacuum solutions to Newcomb's equation, and are defined in Ref. 23.

Now, we do not expect the above torque to interfere with the previously described mutual phase-locking of the $m=0$ and $m=1$ modes within the plasma (see Sec. V D). However, in the large mode amplitude limit, we do expect the phase of the 0, 1 mode to adjust itself such that the absolute magnitude of T_*' is minimized. From Eq. (50), this implies that $\varphi^{0,1} = \varphi_v^{0,1}$ (the solution $\varphi^{0,1} = \varphi_v^{0,1} + \pi$ is dynamically unstable), which, from Eq. (35), yields

$$\phi_0 = \varphi_v^{0,1} + \Delta_0, \qquad (52)$$

with $\Delta_0 = \pm \pi/2$. Thus, we conclude that the peak of the $m=0$ slinky pattern (located at $\phi = \phi_0$) locks 90° out of phase with a strong 0,1 error-field. Clearly, if the error-field is stationary then the rotation of the $m=0$ component of the slinky pattern, and all its constituent $m=0$ modes, is arrested. Note, however, that although the rotation of the $m=1$ component of the slinky pattern (which peaks at $\phi = \phi_1$) is also arrested (since ϕ_1 is tied to ϕ_0 via three-wave coupling), in general, the pattern's constituent $m=1$ modes continue to rotate. In fact, as can be seen from Eq. (42), in this case, the angular phase velocities of all the coupled $m=1$ modes become equal: i.e., $\dot{\varphi}^{1,n} = -d\Delta_1/dt$. Note that we can talk about the time derivative of Δ_1 because this quantity does not have a fixed value in our theory, unlike Δ_0.

A stationary slinky pattern which is phase-locked to a static 0, 1 error-field can be forced to propagate via the application of an externally generated, rotating, 0, 1 magnetic perturbation. Suppose, for the sake of simplicity, that the phase of the static error-field is 0°. In the large amplitude limit, the phase of the $m=0$ component of the slinky pattern becomes

$$\phi_0 = \tan^{-1}\left(\frac{a_r \sin \varphi_r}{1 + a_r \cos \varphi_r}\right) + \Delta_0, \tag{53}$$

where a_r is the amplitude of the rotating perturbation (relative to the amplitude of the static error-field), and $\varphi_r(t)$ is the phase of the perturbation. Thus, as long as the amplitude of the rotating perturbation remains less than that of the error-field (i.e., $a_r < 1$), the slinky pattern oscillates in phase, but does not rotate. However, as soon as the amplitude of the perturbation exceeds that of the error-field (i.e., $a_r > 1$), the pattern is forced to rotate. The rotation is very uneven if a_r is close to unity, with the phase velocity of the pattern slowing down when $\varphi_r \simeq 0°$, and speeding up when $\varphi_r \simeq 180°$. However, if the amplitude of the applied perturbation becomes very large (i.e., $a_r \gg 1$), the $m=0$ component of the slinky pattern is forced to co-rotate exactly with the perturbation, but the peak of the pattern always remains 90° out of phase with the perturbation.

C. Phase-locking to an $m=1$ error-field

As we have seen, a static $m=0$ error-field is capable of arresting the rotation of the slinky pattern, and its constituent $m=0$ modes, but cannot prevent the constituent $m=1$ modes from rotating. In order to arrest the rotation of the $m=1$ modes, it is necessary for at least one of these modes to phase-lock to a static $m=1$ error-field.

Consider the effect of a 1, n_0 error-field of amplitude Ψ_v^{1,n_0} and phase φ_v^{1,n_0}. The additional flux-surface averaged, radially integrated, toroidal torque generated at the 1, n_0 rational surface is written[18]

$$(T_\phi^{1,n_0})' = -\frac{2\pi^2 R_0}{\mu_0} \frac{n_0}{1 + n_0^2 \epsilon_s^2}$$
$$\times E_{sc}^{1,n_0} \Psi_v^{1,n_0} \Psi^{1,n_0} \sin(\varphi^{1,n_0} - \varphi_v^{1,n_0}). \tag{54}$$

The associated additional poloidal torque satisfies $(T_\theta^{1,n_0})' = -(T_\phi^{1,n_0})'/n_0$.

As before, we do not expect the above torque to interfere with the mutual phase-locking of the $m=0$ and $m=1$ modes within the plasma (see Sec. V D). However, in the large mode amplitude limit, we do expect the phase of the 1, n_0 mode to adjust itself such that the absolute magnitude of $(T_\phi^{1,n_0})'$ is minimized. Clearly, this implies

$$\varphi^{1,n_0} = \varphi_v^{1,n_0} \tag{55}$$

(the solution $\varphi^{1,n_0} = \varphi_v^{1,n_0} + \pi$ is dynamically unstable). Now, if the 1, n_0 error-field is static, and the slinky pattern is phase-locked to a static 0, 1 error-field, then both φ^{1,n_0} and ϕ_1 are constant in time. It follows, from Eq. (42), that the rotation of all the constituent $m=1$ modes is arrested.

Suppose that the slinky pattern, and all of its constituent modes, are rendered nonrotating via phase-locking to a combination of static 0, 1 and 1, n_0 error-fields. Suppose, further, that the pattern is then forced to propagate via the imposition of a large amplitude, rotating, 0, 1 magnetic perturbation. How do the phases of the constituent $m=0$ and $m=1$ modes vary in time? Well, the rotating perturbation generates a torque at the reversal surface which forces the slinky pattern to co-rotate. However, the 1, n_0 mode remains phase-locked to the static 1, n_0 error-field—the rotating perturbation cannot affect this locking, since it generates no torque at the 1, n_0 rational surface. As before, we do not expect the error-field torques to modify the mutual phase-locking of the $m=0$ and $m=1$ modes (see Sec. V D). It follows, from Eqs. (35) and (42), that

$$\dot{\varphi}^{0,k} = k\dot{\varphi}_0, \tag{56}$$

$$\dot{\varphi}^{1,n} = (n - n_0)\dot{\varphi}_0, \tag{57}$$

where $\dot{\varphi}_0 = \dot{\varphi}_1$ is the externally imposed angular phase velocity of the slinky pattern. Here, we have set $d\Delta_1/dt = n_0\dot{\varphi}_1$, in order to ensure that the 1, n_0 mode remains stationary. Clearly, the constituent $m=0$ and $m=1$ modes are forced to rotate with angular phase velocities which are *integer multiples* of the externally imposed angular phase velocity of the slinky pattern. It is interesting to note, however, that $m=1$ modes with $n < n_0$ are forced to rotate in the *opposite direction* to the slinky pattern.

D. Summary

We have seen that in the presence of *single harmonic* $m=0$ and $m=1$ error-fields the rotation of the slinky pattern, and its constituent tearing modes, is modified, but the integrity of the pattern remains unaffected. The reason for this is that the $m=0$ and $m=1$ internal phase-locking constraints, Eqs. (35) and (42), retain sufficient free parameters (i.e., ϕ_0 and Δ_1) that it is possible to specify the phase of a single $m=0$ and a single $m=1$ mode without violating these constraints. Conversely, we expect *multi-harmonic* $m=0$ and $m=1$ error-fields to affect the integrity of the slinky pattern, since, in general, there will be a conflict between the internal phase relations, Eqs. (35) and (42), and those imposed externally by the error-fields.

VI. COMPARISON WITH EXPERIMENTAL DATA

A. Introduction

In this section, we shall compare the theoretical predictions of Secs. III and IV with the mode locking phenomenology observed in the RFX experiment[5] (major radius, $R_0 = 2.0$ m; vacuum vessel internal and external radii, $r_{int} = a = 0.457$ m and $r_{ext} = 0.505$ m; stabilizing shell internal and external radii, $c_{int} = 0.538$ m and $c_{ext} = 0.6$ m). The main characteristics of mode locking in RFX were described in Ref. 19. Here, we present an extended and more tightly focused version of this analysis.
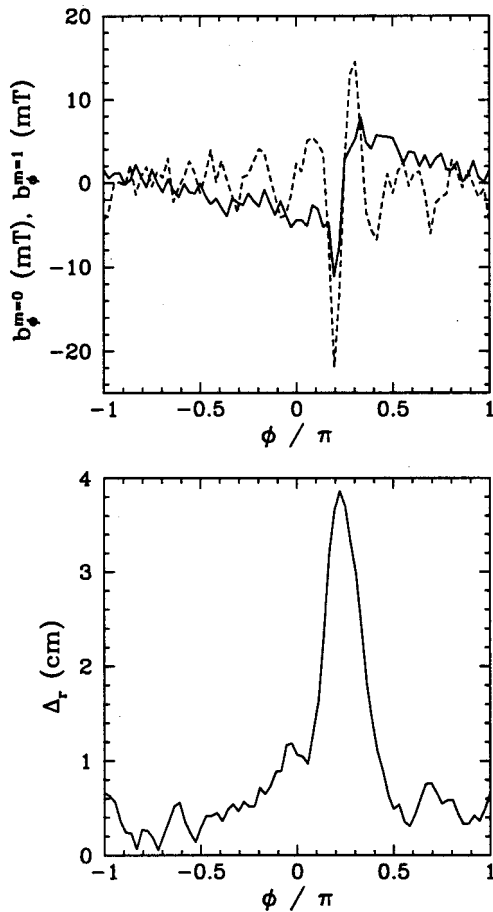
FIG. 5. Typical $m=0$ (solid curve) and $m=1$ (dashed curve) contributions to the perturbed toroidal magnetic field in RFX (shot 8071, time 9 ms). Also shown (bottom panel) is the radial displacement of the plasma boundary associated with the $m=1$ perturbation.

B. Analysis

All RFX discharges are characterized by a large amplitude, stationary, toroidally localized magnetic perturbation.[28] This perturbation is made up of phase-locked $m=0$ and $m=1$ modes with a broad spectrum of toroidal mode numbers.[19] Presumably, the perturbation is stationary, rather than rotating, because its constituent modes are locked to static error-fields. Error-field locking is greatly facilitated by eddy currents excited in the thin resistive vacuum vessel.[14,15]

The RFX magnetic perturbation is mainly analyzed using signals provided by two toroidal arrays of magnetic pick-up coils, which measure the toroidal component of the magnetic field. Each array consists of 72 equally spaced coils. Hence, toroidal harmonics up to $n=36$ can be resolved. The arrays are situated between the vacuum vessel and the stabilizing shell, on the inner surface of the shell. The "inboard" and "outboard" arrays are located at poloidal angles $\theta_{in}=-20.5°$ and $\theta_{out}=159.5°$, respectively (the inboard mid-plane corresponds to $\theta=0°$). Thus, the contribution of the $m=0$ and $m=1$ modes can be distinguished by taking sums and differences, respectively, of the signals emanating from these two arrays.

The typical toroidal profiles of the $m=0$ and $m=1$ contributions to the perturbed toroidal field are shown in Fig. 5
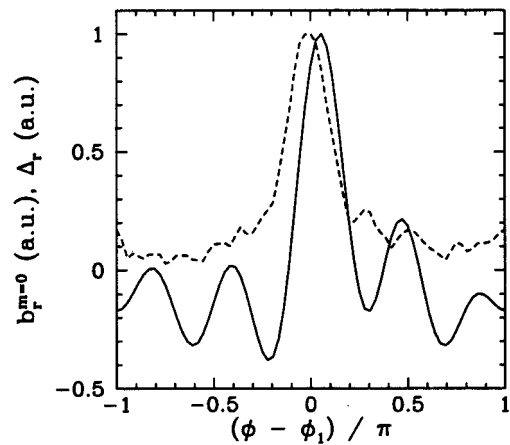

FIG. 6. Typical $m=0$ contribution to the perturbed radial field (solid curve) in RFX (average over many similar discharges). Also shown (dashed curve) is the radial displacement of the plasma boundary associated with the $m=1$ perturbation.

(shot 8071, time 9 ms). A systematic wave form due to eddy currents flowing in the RFX conducting shell has been subtracted out of the $m=0$ profile.[29] Actually, the $m=1$ perturbation is best represented as a helical displacement, $\Delta_r(\phi)$ (also shown in Fig. 5), of the plasma surface in the radial direction.[11] As demonstrated in Ref. 19, the maximum of $\Delta_r(\phi)$ corresponds to the peak amplitude of the $m=1$ perturbation (i.e., to the angle $\phi=\phi_1$).

The $m=0$ profile, $b_\phi^{m=0}(\phi)$, exhibits a linear trend, with a quasi-discontinuity. Thus, this profile is in excellent agreement with the predictions of Sec. III. In all discharges examined, $b_\phi^{m=0}(\phi)$ *decreases* linearly with ϕ, which is consistent with our theoretical $m=0$ phase-locking formula (35), provided $\Delta_0=\pi/2$. Moreover, the maximum of $\Delta_r(\phi)$ occurs at an angle, ϕ_1, which is close to, but slightly *less than*, the angle ϕ_0 at which the $b_\phi^{m=0}(\phi)$ discontinuity passes through zero. On the one hand, this confirms that the phase-locking of the $m=1$ modes is due to interaction with the $m=0$ modes. On the other hand, the sign of the offset between ϕ_0 and ϕ_1 suggests that the overlap integrals which characterize the nonlinear coupling between the various $m=0$ and $m=1$ modes are generally *negative* in RFX (see Sec. IV).

As discussed in Sec. III, phase-locking with $\Delta_0=\pi/2$ is expected to lead an $m=0$ radial field with a positive spike at toroidal angle $\phi=\phi_0$. Unfortunately, the $m=0$ radial field can not be measured on a shot to shot basis in RFX, due to the absence of similar toroidal arrays of radial field probes. However, the average $b_r^{m=0}(\phi)$ profile can be calculated via a statistical analysis made on many similar discharges.[29] This technique involves the reconstruction of the $m=0$ toroidal flux perturbation, $\psi_\phi^{m=0}(\phi)$, using data from four toroidal flux loops located on the outer surface of the vacuum vessel. The corresponding $m=0$ radial magnetic field is given by $b_r^{m=0}(\phi)=-(1/2\pi r R_0)\ (\partial\psi_\phi^{m=0}/\partial\phi)$. The normalized $b_r^{m=0}(\phi)$ profile shown in Fig. 6 is the result of a fit performed using the first 6 toroidal harmonics (the amplitudes of all these harmonics are comparable). Our analysis confirms the presence of an $m=0$ radial field with a positive
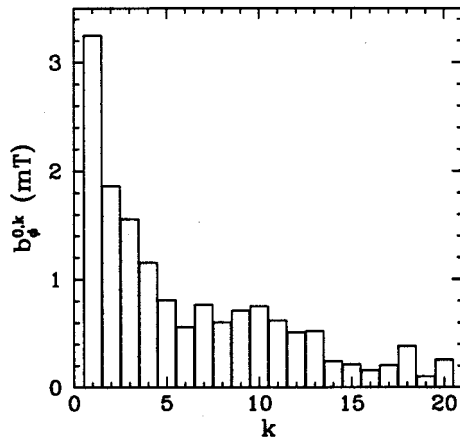
FIG. 7. Typical Fourier amplitudes of the $m=0$ contributions to the perturbed toroidal magnetic field in RFX (shot 8071, time 9 ms).

FIG. 9. The functions $d_0(k)=\varphi^{0,k+1}-\varphi^{0,k}-\varphi^{0,1}$ versus k for a typical, fully phase-locked, magnetic perturbation in RFX (shot 8071, time 9 ms).

spike at an angle slightly greater than $\phi=\phi_1$. This result is fully consistent with our theoretical predictions.

Figure 7 and 8 show the typical Fourier amplitudes of the $m=0$ and $m=1$ contributions to the perturbed toroidal magnetic field in RFX (shot 8071, time 9 ms). As can be seen, the dominant $m=0$ amplitudes correspond to k in the range 1–13, whereas the dominant $m=1$ amplitudes correspond to n in the range 7–15.

Figures 9 and 10 plot the functions

$$d_0(k)=\varphi^{0,k+1}-\varphi^{0,k}-\varphi^{0,1}, \tag{58}$$

$$d_1(n)=\varphi^{1,n+1}-\varphi^{1,n}-\varphi^{0,1}, \tag{59}$$

for a typical, fully phase-locked, magnetic perturbation in RFX (shot 8071, time 9 ms). Our theoretical phase-locking relations, Eqs. (35) and (42), predict $d_0(k)=\Delta_0$ and $d_1(n)=\phi_1-\phi_0+\Delta_0$. Since we have already determined that $\Delta_0=\pi/2$ and $0<\phi_0-\phi_1\ll\pi$ in RFX, we expect the $d_0(k)$ to take the constant value $\pi/2$, and the $d_1(n)$ to take a constant value slightly less than $\pi/2$. From Figs. 9 and 10, it can be seen that these expectations are largely borne out for the dominant modes.
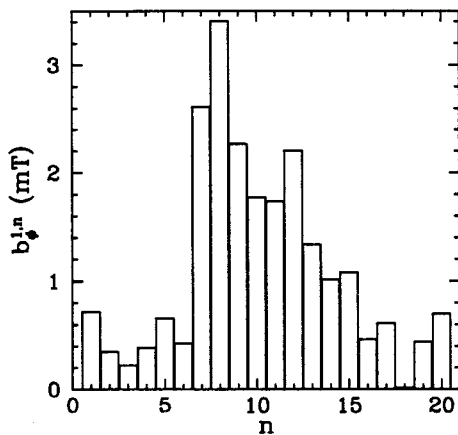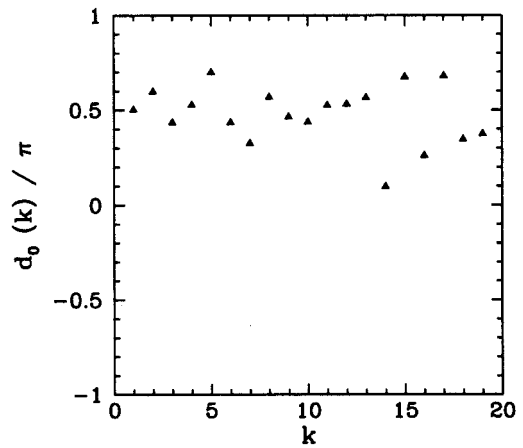
Figure 11 shows the typical time evolution of the (odd-k) 0, k Fourier amplitudes of the perturbed toroidal magnetic field in RFX (shot 8071). In this example, the equilibrium edge toroidal magnetic field reverses sign at time $t_{\text{rev}}=4.8$ ms. The $m=0$ modes can be seen to undergo a fast growth phase shortly after reversal. Note that every curve in Fig. 11 is normalized with respect to its value at the end of the growth phase. Now, the slope of each curve gives an estimate of the growth-rate of the associated $m=0$ harmonic. It can be seen that the growth-rates are all very similar. (Note that the slope of the signals is affected by the presence of the resistive vacuum vessel, which tends to slow down the growth of the lower k modes.) The similarity of the growth-rates justifies our earlier assumption, in Sec. III, of a common time dependence of the $m=0$ modes. Incidentally, the growth phase of the $m=1$ modes (not shown) starts a little before the reversal time.

Figure 12 shows typical temporal traces of the functions $d_0(k)=\varphi^{0,k+1}-\varphi^{0,k}-\varphi^{0,1}$ in RFX. Data are plotted for the five most important $m=0$ modes; i.e., $k=1-5$. It can be seen that as the $m=0$ modes grow in amplitude they undergo phase-locking characterized by $d_0(k)\rightarrow\pi/2$. The behavior

FIG. 8. Typical Fourier amplitudes of the $m=1$ contributions to the perturbed toroidal magnetic field in RFX (shot 8071, time 9 ms).
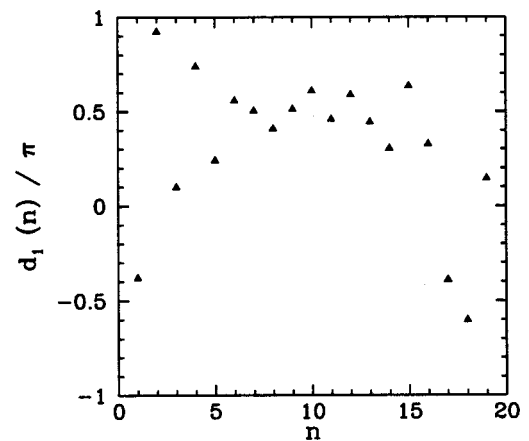

FIG. 10. The functions $d_1(n)=\varphi^{1,n+1}-\varphi^{1,n}-\varphi^{0,1}$ versus n for a typical, fully phase-locked, perturbation in RFX (shot 8071, time 9 ms).
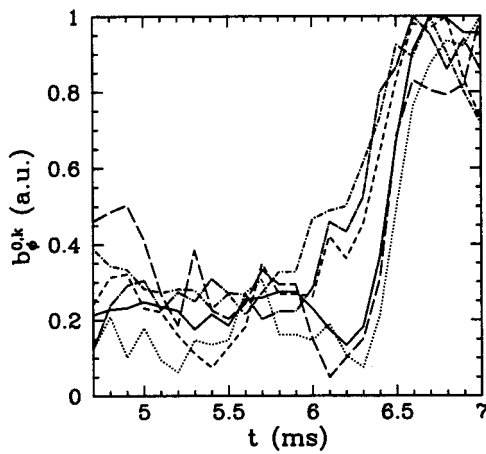
FIG. 11. Typical time evolution of the (odd-k) 0, k Fourier amplitudes of the perturbed toroidal magnetic field in RFX (shot 8071). Each curve is normalized with respect to its value at the end of the growth phase. The solid curve corresponds to $k=1$, the dotted curve to $k=3$, the short-dashed curve to $k=5$, the long-dashed curve to $k=7$, the dot–short-dashed curve to $k=9$, and the dot–long-dashed curve to $k=11$.

seen in Fig. 12 is consistent with our hypothesis, developed in Sec. III, that $m=0$ phase-locking involves the minimization of the magnitude of the electromagnetic torque at the reversal surface, triggered by high mode amplitudes.

Figure 13 shows typical temporal traces of the functions $d_1(n)=\varphi^{1,n+1}-\varphi^{1,n}-\varphi^{0,1}$ in RFX. Data are plotted for the five most important $m=1$ modes; i.e., $n=7-11$. As can be seen, when the $m=0$ (and $m=1$) mode amplitudes are high, the nonlinear interaction of the $m=0$ and $m=1$ modes leads to a phase-locked configuration in which the $d_1(n)$ are (on average) slightly less than $\pi/2$. This behavior is in complete accordance with our theoretical predictions.

C. Summary

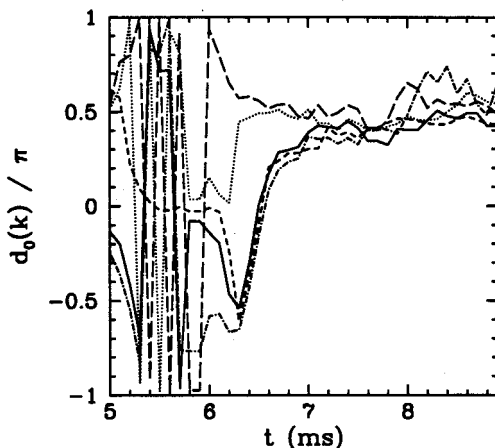The theoretical predictions of Secs. III and IV are in excellent agreement with the mode locking phenomenology

FIG. 12. Typical temporal traces of the functions $d_0(k)=\varphi^{0,k+1}-\varphi^{0,k}-\varphi^{0,1}$, for $k=1-5$, in RFX (shot 8071). The solid curve corresponds to $k=1$, the dotted curve to $k=2$, the short-dashed curve to $k=3$, the long-dashed curve to $k=4$, and the dot–short-dashed curve to $k=5$.
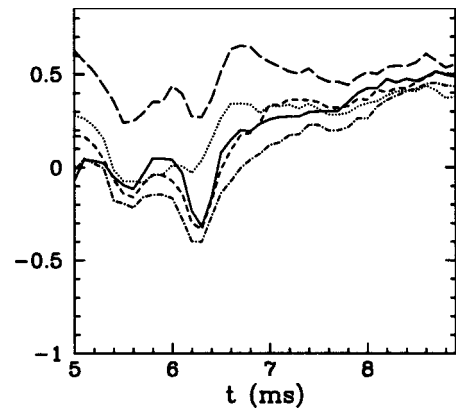

FIG. 13. Typical temporal traces of the functions $d_1(n)=\varphi^{1,n+1}-\varphi^{1,n}-\varphi^{0,1}$, for $n=7-11$, in RFX (shot 8071). The solid curve corresponds to $n=7$, the dotted curve to $n=8$, the short-dashed curve to $n=9$, the long-dashed curve to $n=10$, and the dot–short-dashed curve to $n=11$.

observed in RFX. In particular, we have successfully explained the observed forms of the edge $b_r^{m=0}(\phi)$ and $b_\phi^{m=0}(\phi)$ profiles. Moreover, we can account for the small offset seen between the locking angle, ϕ_0, of the $m=0$ modes, and the corresponding angle, ϕ_1, of the $m=1$ modes. Finally, our theoretical phase-locking relations, Eqs. (35) and (42), appear to be highly consistent with the experimental data.

VII. PHASE EVOLUTION EQUATIONS

A. Introduction

The previous theoretical analysis can be improved. In the following, we present a set of phase evolution equations which model the phase-locking of tearing modes in an RFP plasma with a fairly high degree of fidelity. We shall employ these equations to make a more exact comparison between our theory and the RFX data presented above. We shall also use our equations to investigate the effect of error-fields on the RFX slinky pattern.

B. Physics content

We assume that the dominant $m=0$ and $m=1$ modes correspond to those which are intrinsically tearing unstable: i.e., those for which $E^{m,n}>0$. Suppose that the intrinsically unstable $m=0$ modes possess toroidal mode numbers in the range 0 to k_0, and that the intrinsically unstable $m=1$ modes possess toroidal mode numbers in the range n_1 to n_2. The various mode amplitudes are specified, whereas the phases are evolved under the influence of the electromagnetic torques (due to three-wave coupling and error-fields) and viscous torques which develop in the plasma. The $m=1$ modes are initialized with random phases, whereas the $m=0$ modes are initialized in a phase-locked configuration (which is not affected by the phase evolution).

The toroidal equation of motion of the plasma is written[25]

$$r\rho\frac{\partial\Omega_\phi}{\partial t} - \frac{\partial}{\partial r}\left(r\mu\frac{\partial\Omega_\phi}{\partial r}\right)$$

$$= \sum_{n=n_1,n_2}\frac{T_\phi^{1,n}}{4\pi^2 R_0^3}\delta(r-r_s^{1,n})$$

$$+ \frac{T_\phi^*}{4\pi^2 R_0^3}\delta(r-r_*) + \frac{rP_\phi}{R_0^2}, \tag{60}$$

where $\Omega_\phi(r,t)$ is the plasma toroidal angular velocity, $\rho(r)$ is the plasma mass density, $\mu(r)$ represents a phenomenological plasma viscosity, and $P_\phi(r)$ is a steady toroidal torque density which maintains the equilibrium plasma rotation. Here, $T_\phi^{1,n}$ is the radially integrated, flux-surface averaged, toroidal electromagnetic torque which develops at the 1, n rational surface due to three-wave coupling. Likewise, T_ϕ^* is the radially integrated, flux-surface averaged, toroidal electromagnetic torque which develops at the reversal surface due to three-wave coupling. Reference 18 explains how the three-wave coupling torques are calculated. The boundary conditions satisfied by the toroidal angular velocity are

$$\frac{\partial\Omega_\phi(0,t)}{\partial r} = \Omega_\phi(a,t) = 0. \tag{61}$$

The poloidal equation of motion of the plasma takes the form[25]

$$r^3\rho\left(\frac{\partial\Omega_\theta}{\partial t} + \frac{\Omega_\theta}{\tau_D}\right) - \frac{\partial}{\partial r}\left(r^3\mu\frac{\partial\Omega_\theta}{\partial r}\right)$$

$$= -\sum_{n=n_1,n_2}\frac{T_\phi^{1,n}}{n4\pi^2 R_0}\delta(r-r_s^{1,n}), \tag{62}$$

where $\Omega_\theta(r,t)$ is the plasma poloidal angular velocity, and τ_D represents a phenomenological poloidal flow damping time. The boundary conditions satisfied by the poloidal angular velocity are

$$\frac{\partial\Omega_\theta(0,t)}{\partial r} = \Omega_\theta(a,t) = 0. \tag{63}$$

The $m=0$ modes are assumed to be phase-locked together, which implies $\varphi^{0,k} = k\varphi^{0,1} + (k-1)\Delta_0$, where $\Delta_0 = \pm\pi/2$. According to standard MHD theory, the m,n tearing mode is convected by the plasma in the immediate vicinity of its rational surface. Such convection gives rise to the familiar "no-slip" condition

$$\frac{d\varphi^{m,n}}{dt} = n\Omega_\phi(r_s^{m,n},t) - m\Omega_\theta(r_s^{m,n},t). \tag{64}$$

Note that the convection of the $m=0$ modes by the plasma in the vicinity of the reversal surface does not affect the mutual phase-locking of these modes.

The model equilibrium current profile adopted in this paper is

$$\sigma(r) = \left(\frac{2\Theta_0}{a}\right)\left[1 - \left(\frac{r}{a}\right)^\alpha\right], \tag{65}$$

where Θ_0 and α are positive constants. It is conventional to parameterize RFP equilibria in terms of the *pinch parameter*,

$\Theta = B_\theta(a)/\langle B_\phi\rangle$, and the *reversal parameter*, $F = B_\phi(a)/\langle B_\phi\rangle$, where $\langle\cdots\rangle$ denotes a volume average.

C. Normalized phase evolution equations

It is convenient to define the following normalized quantities: $\hat{r} = r/a$, $\hat{t} = t\Omega_\phi^{(0)}(0)$, $\hat{\mu} = \mu/\mu(0)$, $\hat{\rho} = \rho/\rho(0)$, $\hat{\Omega}_\phi = \Omega_\phi/\Omega_\phi^{(0)}(0)$, $\hat{\Omega}_\theta = \Omega_\theta/\Omega_\phi^{(0)}(0)$, $\hat{r}_n = r_s^{1,n}/a$, $\hat{r}_* = r_*/a$, $F_*' = (dF^{0,1}/dr)_{r_*}$, $P_{n,k} = (\epsilon_*^2 r_*^2 F_*'/4)\mathcal{P}\int_0^a t_{n,k}dr$, $\tau_H = [\mu_0\rho(0)]^{1/2}/F_*'$, $\tau_V = a^2\rho(0)/\mu(0)$, $\nu = 1/[\tau_V\Omega_\phi^{(0)}(0)]$, $\gamma_D = \tau_V/\tau_D$, $\Lambda = [2\tau_H^2\Omega_\phi^{(0)}(0)/\tau_V\hat{r}_*^2]^{1/3}$, $A^{1,n} = \Psi^{1,n}/(\Lambda r_*^2 F_*')$, and $A^{0,k} = \Psi^{0,k}/(\Lambda r_*^2 F_*')$. Here, $\Omega_\phi^{(0)}(0)$ is the unperturbed, steady-state, plasma toroidal angular velocity on the magnetic axis.

It is helpful to define a set of toroidal velocity eigenfunctions, $u_j(\hat{r})$, and eigenvalues, β_j:

$$\frac{d}{d\hat{r}}\left(\hat{r}\hat{\mu}\frac{du_j}{d\hat{r}}\right) + \hat{r}\hat{\rho}\beta_j u_j = 0, \tag{66}$$

$$\frac{du_j(0)}{d\hat{r}} = u_j(1) = 0, \tag{67}$$

$$\int_0^1 \hat{r}\hat{\rho}u_j u_k d\hat{r} = \delta_{jk}. \tag{68}$$

Likewise, it is helpful to define a set of poloidal velocity eigenfunctions, $v_j(\hat{r})$, and eigenvalues, γ_j:

$$\frac{d}{d\hat{r}}\left(\hat{r}^3\hat{\mu}\frac{dv_j}{d\hat{r}}\right) + \hat{r}^3\hat{\rho}\gamma_j v_j = 0, \tag{69}$$

$$\frac{dv_j(0)}{d\hat{r}} = v_j(1) = 0, \tag{70}$$

$$\int_0^1 \hat{r}^3\hat{\rho}v_j v_k d\hat{r} = \delta_{jk}. \tag{71}$$

Our phase evolution equations take the form

$$\frac{d\varphi^{1,n}}{d\hat{t}} = \sum_{j=1,\infty}\left[\sum_{n'=n_1,n_2}ng_{n',j}u_j(\hat{r}_n)\right.$$

$$\left. + ng_{*,j}u_j(\hat{r}_n) - \sum_{n'=n_1,n_2}f_{n',j}v_j(\hat{r}_n)\right], \tag{72}$$

$$\frac{d\varphi^{0,1}}{d\hat{t}} = \sum_{j=1,\infty}\left[\sum_{n'=n_1,n_2}g_{n',j}u_j(\hat{r}_*) + g_{*,j}u_j(\hat{r}_*)\right], \tag{73}$$

$$\varphi^{0,k} = k\varphi^{0,1} + (k-1)\Delta_0, \tag{74}$$

where $\Delta_0 = \pm\pi/2$. Here,

$$\frac{1}{\nu}\frac{dg_{n,j}}{d\hat{t}} = \hat{T}_\phi^{1,n}u_j(\hat{r}_n) + p_j - \beta_j g_{n,j}, \tag{75}$$

$$\frac{1}{\nu}\frac{dg_{*,j}}{d\hat{t}} = \hat{T}_\phi^* u_j(\hat{r}_*) + p_j - \beta_j g_{*,j}, \tag{76}$$

$$\frac{1}{\nu}\frac{df_{n,j}}{d\hat{t}} = -\frac{\hat{T}_{\phi}^{1,n}v_j(\hat{r}_n)}{n\epsilon_a^2} - (\gamma_j + \gamma_D)f_{n,j}, \tag{77}$$

and $p_j = \int_0^1 \hat{r}u_j(\hat{r})\hat{P}_\phi(\hat{r})d\hat{r}$, where $\hat{P}_\phi = P_\phi/P_0$, and P_0 is adjusted such that $\hat{\Omega}_\phi(0) = 1$ in unperturbed steady-state. Finally,

$$\hat{T}_{\phi}^{1,n} = -\sum_{k=1}^{\min(n_2-n,k_0)} n\hat{T}_{n,k} + \sum_{k=1}^{\min(n-n_1,k_0)} n\hat{T}_{n-k,k}, \tag{78}$$

$$\hat{T}_{\phi}^* = -\sum_{k=1}^{k_0}\sum_{n=n_1}^{n_2-k} k\hat{T}_{n,k}, \tag{79}$$

where

$$\hat{T}_{n,k} = P_{n,k}A^{1,n+k}A^{1,n}A^{0,k}$$
$$\times \sin(\varphi^{1,n+k} - \varphi^{1,n} - \varphi^{0,k}). \tag{80}$$

Note that the toroidal electromagnetic torques exerted on the 1, n, the 1, $n+k$, and the 0, k rational surfaces, due to three-wave coupling of the corresponding tearing modes, are in the ratio $-n$: $n+k$: $-k$. Likewise, the associated poloidal torques are in the ratio 1: -1: 0 (with the same constant of proportionality as the toroidal torques).

In the presence of a 0, 1 error-field, the normalized toroidal torque at the reversal surface increases by

$$(\hat{T}_{\phi}^*)' = -A^{0,1}B^{0,1}\sin(\varphi^{0,1} - \varphi_v^{0,1}), \tag{81}$$

where

$$B^{m,n} = \frac{\epsilon_*^2}{m^2 + n^2\epsilon_s^2}\frac{E_{sc}^{m,n}\Psi_v^{m,n}}{r_*^2F_*'\Lambda^2}. \tag{82}$$

Likewise, in the presence of a 1, n_0 error-field, the toroidal torque at the 1, n_0 rational surface increases by

$$(\hat{T}_{\phi}^{1,n_0})' = -n_0 A^{1,n_0}B^{1,n_0}\sin(\varphi^{1,n_0} - \varphi_v^{1,n_0}). \tag{83}$$

The $\varphi^{1,n}$ and $\varphi^{0,1}$ are given random initial values, whereas the plasma velocity profile is initialized in an unperturbed steady-state: i.e., $g_{n,j} = p_j/\beta_j$, $g_{*,j} = p_j/\beta_j$, $f_{n,j} = 0$. The following density, viscosity, and momentum input profiles are adopted:

$$\hat{\rho}(\hat{r}) = (1 - \hat{r}^2)^{\gamma_\rho}, \tag{84}$$

$$\hat{\mu}(\hat{r}) = (1 + \hat{r}^2)^{\gamma_\mu}, \tag{85}$$

$$\hat{P}_\phi(\hat{r}) = \hat{P}_\phi(0)(1 - \hat{r}^2)^{\gamma_p}, \tag{86}$$

where $\hat{P}_\phi(0)$ is adjusted such that $\hat{\Omega}_\phi(0) = \sum_{j=1}^{\infty}p_j u_j(0)/\beta_j = 1$.

D. Edge magnetic fields

The $m=0$ radial and toroidal magnetic-field perturbations at the plasma edge take the form

$$\frac{b_r^{m=0}(\phi)}{b_0} = \mathrm{sgn}(\Delta_0)\sum_{k=1}^{k_0} A^{0,k}\hat{b}_r^{0,k}\cos[k(\phi - \phi_0)], \tag{87}$$

$$\frac{b_\phi^{m=0}(\phi)}{b_0} = -\mathrm{sgn}(\Delta_0)\sum_{k=1}^{k_0} A^{0,k}\hat{b}_\phi^{0,k}\sin[k(\phi - \phi_0)], \tag{88}$$

where $b_0 = \Lambda r_*^2 F_*'/a$, and

$$\hat{b}_r^{m,n} = \hat{\psi}^{m,n}(1), \tag{89}$$

$$\hat{b}_\phi^{m,n} = \frac{n\epsilon_a(d\hat{\psi}_{m,n}/d\hat{r})(1)}{m^2 + n^2\epsilon_a^2}. \tag{90}$$

The $m=1$ radial and toroidal magnetic field perturbations at the plasma edge are written

$$\frac{b_r^{m=1}(\theta,\phi)}{b_0} = \cos\theta\, F_r^C(\phi) + \sin\theta\, F_r^S(\phi), \tag{91}$$

$$\frac{b_\phi^{m=1}(\theta,\phi)}{b_0} = \cos\theta\, F_\phi^C(\phi) + \sin\theta\, F_\phi^S(\phi), \tag{92}$$

where

$$F_r^C(\phi) = \sum_{n=n_1}^{n_2} A^{1,n}\hat{b}_r^{1,n}\sin(n\phi - \varphi^{1,n}), \tag{93}$$

$$F_r^S(\phi) = -\sum_{n=n_1}^{n_2} A^{1,n}\hat{b}_r^{1,n}\cos(n\phi - \varphi^{1,n}), \tag{94}$$

$$F_\phi^C(\phi) = \sum_{n=n_1}^{n_2} A^{1,n}\hat{b}_\phi^{1,n}\cos(n\phi - \varphi^{1,n}), \tag{95}$$

$$F_\phi^S(\phi) = \sum_{n=n_1}^{n_2} A^{1,n}\hat{b}_\phi^{1,n}\sin(n\phi - \varphi^{1,n}). \tag{96}$$

Finally, the $m=1$ radial displacement of the plasma torus, Δ_r, is proportional to the magnitude of $b_r^{m=1}$ at the plasma edge;[30] hence,

$$\Delta_r(\phi) \propto \sqrt{(F_r^C)^2 + (F_r^S)^2}. \tag{97}$$

E. Mode amplitudes

In this paper, the mode amplitudes are specified, rather than calculated. Let

$$A^{1,n} = A^{1/3}A_0^{-1/3}\hat{A}^{1,n}, \tag{98}$$

$$A^{0,k} = A^{1/3}A_0^{2/3}\hat{A}^{0,k}, \tag{99}$$

where $\hat{A}^{1,n_1} = \hat{A}^{0,1} = 1$, and $A_0 = \Psi^{0,1}/\Psi^{1,n_1}$. The assumed common time dependence of the mode amplitudes is parameterized via the function

$$A(\hat{t}) = A_{\max}[1 - \exp(-\hat{t}/\hat{t}_{\mathrm{on}})], \tag{100}$$

where $A_{\max}$ is made sufficiently large that electromagnetic torques dominate viscous torques and plasma inertia in the final state. The relative mode amplitudes, $\hat{A}^{1,n}$ and $\hat{A}^{0,k}$, are simply determined from experimental data. It follows that:

$$A^{1,n+k}A^{1,n}A^{0,k} = A\hat{A}^{1,n+k}\hat{A}^{1,n}\hat{A}^{0,k}, \tag{101}$$

$$A^{0,1}B^{0,1} = A^{1/3}\hat{B}^{0,1}, \tag{102}$$

$$A^{1,n_0}B^{1,n_0} = A^{1/3}\hat{B}^{1,n_0}\hat{A}^{1,n_0}, \tag{103}$$

where $\hat{B}^{0,1} = B^{0,1}A_0^{2/3}$ and $\hat{B}^{1,n_0} = B^{1,n_0}/A_0^{1/3}$.

TABLE II. The normalized overlap integrals, $P_{n,k}$, for the modes used in the phase-locking simulation of RFX shot 8071.

k/n	8	9	10	11	12	13
1	2.815e+0	9.809e−1	6.295e−1	4.650e−1	3.643e−1	2.944e−1
2	2.139e+0	8.286e−1	5.547e−1	4.183e−1	3.315e−1	⋯
3	1.798e+0	7.263e−1	4.963e−1	3.785e−1	⋯	⋯
4	1.570e+0	6.473e−1	4.473e−1	⋯	⋯	⋯
5	1.395e+0	5.816e−1	⋯	⋯	⋯	⋯
6	1.250e+0	⋯	⋯	⋯	⋯	⋯

F. Mode-locking simulation

In this subsection, we present a mode-locking simulation of RFX shot 8071 (i.e., the discharge featured in Figs. 5–13). We set $\Delta_0 = \pi/2$ for consistency with the data presented in Sec. VI. Now, the appropriate equilibrium parameters for shot 8071 (at time $t = 9$ ms) are $\epsilon_a = 0.23$, $c = 1.17a$, $F = -0.2$, and $\alpha = 6$. Unfortunately, we find no unstable $m = 1$ modes for these parameters. (Note that the tearing stability indices, $E^{m,n}$, are determined from the plasma equilibrium via Newcomb's equation.) The basic problem is the lack of plasma pressure in our equilibrium model. However, we can crudely compensate for the absence of a destabilizing pressure gradient by increasing the current gradient (i.e., by decreasing α). We find that decreasing α to 3 yields about the correct number of unstable $m = 1$ modes. The unstable $m = 1$ modes have toroidal mode numbers in the range $n = 8-14$. The unstable $m = 0$ modes (which couple to the $m = 1$ modes) have toroidal mode numbers in the range $k = 1-6$. Table I shows some of the key parameters for the modes included in our simulation.

Table II displays the normalized overlap integrals for the modes included in our simulation. It can be seen that all the integrals are *positive*. This sign for the integrals is in conflict with the data presented in Sec. VI, where it was determined that the integrals are generally negative in RFX. We conjecture that the origin of the inconsistency is our inaccurate model for the plasma equilibrium. We find that the dominant contribution to the overlap integrals comes from the region of the plasma lying outside the reversal surface—unfortunately, our model equilibrium is particularly unrealistic in this region. Furthermore, the overlap integrals are made up of sums of finely balanced terms, each much larger in magnitude that the integrals themselves. Thus, it appears plausible that a more accurate equilibrium model, including plasma pressure, could reverse the signs of the integrals. Unfortunately, the incorporation of plasma pressure would lead to a very considerable increase in the complexity of our model, and is not attempted in this paper.

The plasma parameters used in our simulation are $\nu = 0.01$, $\gamma_D = 10$, $\gamma_\rho = 0.5$, $\gamma_\mu = 3$, and $\gamma_p = 2$. Note that the final phase-locked configuration of the $m = 0$ and $m = 1$ modes is completely insensitive to these parameters. This insensitivity accords well with our fundamental hypothesis that the final configuration is determined almost entirely by electromagnetic torques, and is only very weakly affected by plasma viscosity, inertia, and poloidal flow damping.

The relative mode amplitudes, $A^{1,n}$ and $A^{0,k}$, are reconstructed from the data shown in Fig. 7, Fig. 8, and Table 1. The common amplitude factor, $A(t)$ [see Eq. (100)], takes the parameters $A_{\max} = 0.01$ and $t_{\mathrm{on}} = 2\tau$, where $\tau = 2\pi/\Omega_\phi^{(0)}(0)$ is the unperturbed toroidal rotation period of the plasma core. The error-field amplitudes $\hat{B}^{0,1}$ and $\hat{B}^{1,n_0}$ are both set to zero. Finally, the simulation is run from $t = 0$ to $t = 10\tau$. We find that, although the various $m = 1$ modes are initialized with random phases, the final phase-locked configuration is always the same. This demonstrates that phase-locking is a robust and reproducible phenomenon.

Figure 14 shows the functions $d_1(n) = \varphi^{1,n+1} - \varphi^{1,n} - \varphi^{0,1}$ versus time for the dominant $m = 1$ modes in our simulation. The behavior seen in this figure is in good agreement with the analysis of Sec. IV. As time progresses, and the ambient mode amplitude gradually increases, the dominant $m = 1$ modes phase-lock together in a configuration such that $d_1(n)$ takes an approximately constant value *slightly greater* than $\pi/2$. Note, however, that the phase-locking is not perfect. In particular, $d_1(13)$ does not quite converge to the same locking angle as the other $d_1(n)$ curves, indicating that the $n = 14$ mode locks in a configuration which does not quite accord with our $m = 1$ mode-locking relation (42). This type of behavior—which is often seen in our simulations—may account for some of the scatter seen in the experimental phase-locking data—see Figs. 9, 10,
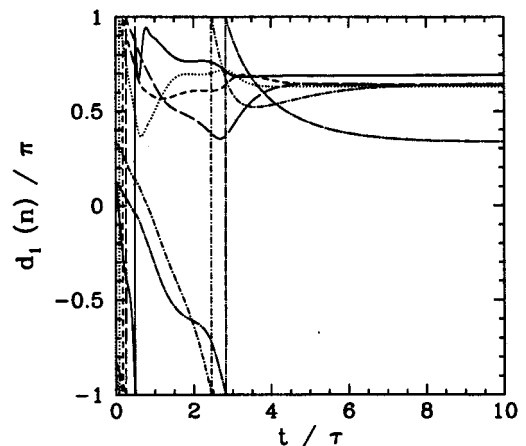

FIG. 14. The functions $d_1(n) = \varphi^{1,n+1} - \varphi^{1,n} - \varphi^{0,1}$ versus time for $n = 8-13$. The solid curve corresponds to $n = 8$, the dotted curve to $n = 9$, the short-dashed curve to $n = 10$, the long-dashed curve to $n = 11$, the dot–short-dashed curve to $n = 12$, and the dot–long-dashed curve to $n = 13$. Data from a phase-locking simulation of RFX shot 8071.
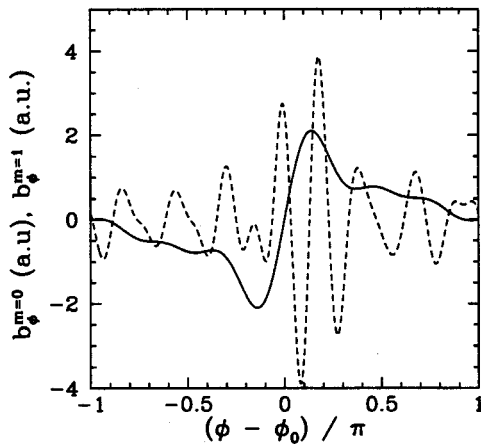
FIG. 15. The final $m=0$ (solid curve) and $m=1$ (dashed curve) contributions to the perturbed edge toroidal magnetic field. Data from a phase-locking simulation of RFX shot 8071.

12, and 13. The simulation data shown in Fig. 14 are fairly consistent with the experimental data displayed in Fig. 13, except for the fact that in the experiment the $d_1(n)$ curves converge to a locking angle *slightly less* than $\pi/2$. This discrepancy is due to the incorrect sign of the overlap integrals in our simulation (see Sec. IV).

Figure 15 shows the final $m=0$ and $m=1$ contributions to the perturbed edge toroidal magnetic field in our simulation. [We have chosen the value of θ used to calculate the $b_\phi^{m=1}$ curve in order to match the experimental data as closely as possible.] The profiles shown in Fig. 15 are similar to the experimental data displayed in Fig. 5. The only major difference is that in the simulation the $m=1$ curve appears slightly shifted to the right, relative to the $m=0$ curve, when compared with the experimental data. This discrepancy is due to the fact that our overlap integrals have the wrong sign.

Figure 16 shows the final $m=0$ contribution to perturbed edge radial magnetic field in our simulation. Also shown is the helical displacement of the plasma boundary due to the
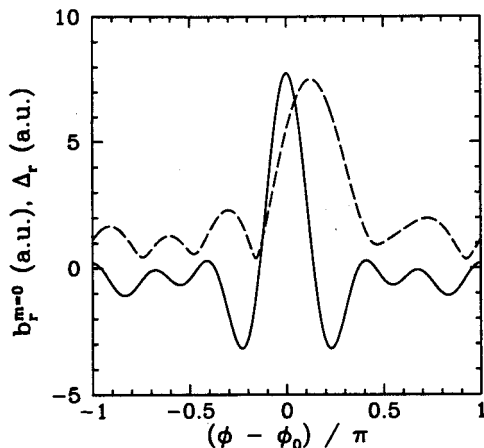

FIG. 16. The final $m=0$ (solid curve) contribution to the perturbed edge radial magnetic field. Also shown in the helical displacement of the plasma boundary due to the $m=1$ modes (dashed curve). Data from a phase-locking simulation of RFX shot 8071.

$m=1$ modes. The profiles shown in Fig. 16 are similar to the experimental data displayed in Fig. 6. In particular, the observed offset between the peaks of the $m=0$ and $m=1$ slinky patterns is reproduced in the simulation. Of course, the offset is in the wrong direction, since our overlap integrals have the incorrect sign.

G. Error-field simulations

The slinky pattern, and its constituent tearing modes, are never observed to spontaneously rotate in RFX. Presumably, the pattern is always phase-locked by static error-fields. As discussed in the Introduction, a nonrotating slinky pattern causes severe edge loading problems. However, in a recent paper, Bartiromo *et al.*[12] reported that the RFX slinky pattern can be forced to propagate via the application of a predominantly 0, 1, rotating, magnetic perturbation. This perturbation is generated by modulating the currents flowing in the toroidal field coils.[13] As expected, the edge loading problems are alleviated, to some extent, as soon as the slinky pattern starts to propagate. In this subsection, we present a couple of rather idealized simulations of this important experiment.

The parameters used in our error-field simulations are the same as those used in the previous simulation, except that the normalized error-field amplitudes, $\hat{B}^{0,1}$ and $\hat{B}^{1,n0}$, are nonzero. We assume that the plasma is subject to static 0,1 and 1,9 error-fields, which are responsible for arresting the rotation of the slinky pattern, and its constituent tearing modes. In addition, the plasma is subject to an externally generated, rotating, 0,1 perturbation, which is intended to force the slinky pattern to propagate. To be more exact

$$\hat{B}^{0,1}=[(B_s^{0,1})^2+2B_s^{0,1}B_r^{0,1}\cos(\varphi_r^{0,1}-\varphi_s^{0,1})+(B_r^{0,1})^2]^{1/2}, \tag{104}$$

$$\varphi_v^{0,1}=\tan^{-1}\left(\frac{B_s^{0,1}\sin\varphi_s^{0,1}+B_r^{0,1}\sin\varphi_r^{0,1}}{B_s^{0,1}\cos\varphi_s^{0,1}+B_r^{0,1}\cos\varphi_r^{0,1}}\right), \tag{105}$$

where $B_s^{0,1}$ and $B_r^{0,1}$ are the normalized amplitudes of the static and rotating 0,1 error-fields, respectively, whereas $\varphi_s^{0,1}$ and $\varphi_r^{0,1}$ are the corresponding phases.

In our simulations, we choose $B_s^{0,1}=20$, $\varphi_s^{0,1}=-\pi/2$, $\hat{B}^{1,9}=20$, and $\varphi_v^{1,9}=0$, which correspond to relatively strong static 0,1 and 1,9 error-fields: i.e., fields capable of locking the slinky pattern in a configuration which is only weakly affected by plasma viscosity and inertia. We also select $\varphi_r^{0,1}=(2\pi/50)(t/\tau)$, which corresponds to a 0,1 perturbation which rotates toroidally 50 times slower than the unperturbed plasma core.

In our first simulation, we set $B_r^{0,1}=20$, which corresponds to a propagating 0,1 perturbation which is only just strong enough to cause the slinky pattern to rotate (see Sec. V). Figure 17 shows the time evolution of the $m=0$ and $m=1$ locking angles, ϕ_0 and ϕ_1. We can see that the slinky pattern rotates very unevenly. Note, in particular, the sudden "jumps" in the pattern phase, by π radians, when the 0,1 plasma mode is in anti-phase with the static 0,1 error-field.
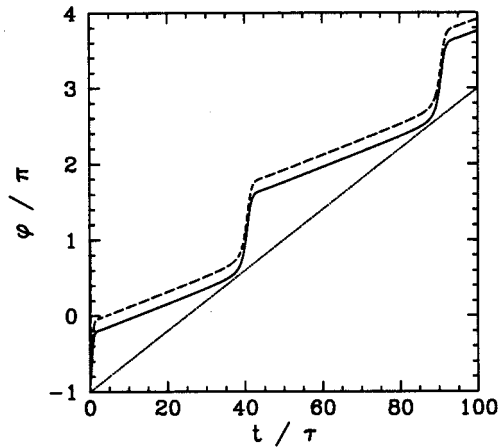
FIG. 17. The $m=0$ locking angle, ϕ_0 (solid curve), the $m=1$ locking angle, ϕ_1 (dashed curve), and the phase of the rotating error-field, $\phi_r^{0,1}$ (dotted curve) versus time. Data from a phase-locking simulation of an RFX shot which includes the effect of static $m=0$ and $m=1$ error-fields, plus a relatively weak, externally generated, rotating, 0,1 magnetic perturbation.

FIG. 19. Time evolution of the $m=1$ phases. The solid curve corresponds to $n=8$, the dotted curve to $n=9$, the short-dashed curve to $n=10$, the long-dashed curve to $n=11$, the dot–short-dashed curve to $n=12$, and the dot–long-dashed curve to $n=14$. Data from a phase-locking simulation of an RFX shot which includes the effect of static $m=0$ and $m=1$ error-fields, plus a relatively strong, externally generated, rotating, 0,1 magnetic perturbation.

Nevertheless, the pattern maintains its integrity as it is pushed around the torus, although there is some variation in $\phi_1-\phi_0$.

In our next simulation, we set $B_r^{0,1}=80$, which corresponds to a propagating 0,1 perturbation which is strong enough to cause the slinky pattern to rotate fairly uniformly (see Sec. V). Figure 18 shows the time evolution of the $m=0$ and $m=1$ locking angles, ϕ_0 and ϕ_1. We can see that the slinky pattern rotates essentially uniformly, but that the $m=0$ locking angle, ϕ_0, is always $\pi/2$ radians out of phase with the perturbation (see Sec. V). Again, the pattern maintains its integrity as it is forced to propagate.

Figure 19 shows the time evolution of the $m=1$ phases in our second simulation. It can be seen that the phase of the 1,9 mode is stationary, since it is locked by the static 1,9 error-field. On the other hand, the 1,8 mode rotates uniformly
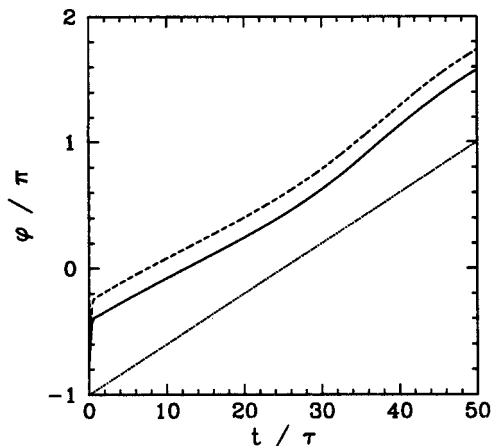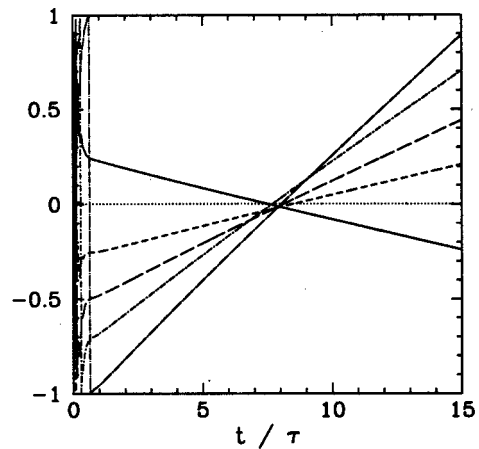
in the *opposite* direction to the slinky pattern, whereas the 1,10 mode rotates uniformly in the *same* direction as the pattern. Note that the magnitudes of the 1,8 and 1,10 angular phase velocities are approximately equal. The 1,11 modes rotates in the same direction as the slinky pattern, but twice as fast as the 1,10 mode. The 1,12 mode rotates three times as fast as the 1,10 mode, etc. (see Sec. V).

The behavior shown in Figs. 17–19 is in *qualitative* agreement with that seen in the RFX mode-rotation experiment (see Figs. 3 and 4 of Ref. 12). However, there are a number of important *quantitative* differences, regarding the phase relation of the slinky pattern to the rotating perturbation, which indicate that our simulations are a little too simplistic. There are two main problems. Firstly, the rotating $m=0$ perturbation used in the RFX mode-rotation experiment appears to have been sufficiently multi-harmonic that it significantly altered the structure of the $m=0$ component of the slinky pattern—indeed there is evidence that $\Delta_0=0$ (rather that $\pm\pi/2$) in the presence of the perturbation. Secondly, the braking torque acting on the slinky pattern due to vacuum vessel eddy currents clearly played an important role in the overall torque balance in the experiment. Neither of these effects were included in our simulations. Nevertheless, the time variation of the $m=1$ phases shown in Fig. 19 is *exactly* the same as that observed in the experiment (see Fig. 4 in Ref. 12). We conjecture that neither of the two complicating factors mentioned above particularly affected the phase-locked configuration of the $m=1$ modes.

H. Summary

Our phase evolution equations are capable of accurately modeling the phase-locking of tearing modes in an RFP plasma. In particular, these equations can be used to predict the properties of the slinky pattern. Our equations can also be employed to deduce the response of this pattern to externally generated, resonant magnetic perturbations.

FIG. 18. The $m=0$ locking angle, ϕ_0 (solid curve), the $m=1$ locking angle, ϕ_1 (dashed curve), and the phase of the rotating error-field, $\phi_r^{0,1}$ (dotted curve) versus time. Data from a phase-locking simulation of an RFX shot which includes the effect of static $m=0$ and $m=1$ error-fields, plus a relatively strong, externally generated, rotating, 0,1 magnetic perturbation.

VIII. SUMMARY AND DISCUSSION

The central hypothesis of this paper is as follows: When the ambient mode amplitude becomes sufficiently high the $m = 0$ and $m = 1$ tearing modes present in an RFP plasma phase-lock together in a configuration which *minimizes* the magnitudes of the electromagnetic torques generated at the various mode rational surfaces. In Sec. III, we demonstrate how this hypothesis enables us to predict the phase-locked configuration of the $m = 0$ modes. Likewise, Sec. IV uses the same hypothesis to determine the phase-locked configuration of the $m = 1$ modes, as well as the locking angle between the $m = 0$ and $m = 1$ contributions to the slinky pattern. Finally, Sec. V explains how our hypothesis leads to predictions regarding the response of the slinky pattern to externally generated, resonant magnetic perturbations.

In Sec. VI, we compare our theoretical predictions with phase-locking data from the RFX experiment. Our theory successfully explains the profiles of the perturbed radial and toroidal magnetic fields at the edge of the plasma, the phase relations between the $m = 0$ and $m = 1$ modes, and the existence of a small toroidal offset between the peaks of the $m = 0$ and $m = 1$ contributions to the slinky pattern.

In Sec. VII, we present a set of phase evolution equations which can be used to model the phase-locking of tearing modes in RFP plasmas, in accordance with our hypothesis. The main benefit of these equations—which is not emphasized in this paper—is that they can be used to make *quantitative* predictions regarding the threshold mode amplitudes required for phase-locking, as well as the threshold error-field strengths needed to arrest the rotation of the slinky pattern.[31] Our phase evolution equations allow us to successfully simulate the phase-locking of tearing modes in RFX. The only significant disagreement between our simulation and the RFX experiment involves the sign of the "overlap integrals" which characterize three-wave coupling between tearing modes. These integrals appear to be negative in RFX, whereas our calculations yield positive integrals. This incorrect sign for the overlap integrals causes us to predict the wrong sign for the toroidal offset between the peaks of the $m = 0$ and $m = 1$ contributions to the slinky pattern. We conjecture that the above mentioned sign problem is associated with the deficiencies of our equilibrium model, which does not take plasma pressure into account.

We have also used our phase evolution equations to successfully simulate the recent RFX mode-rotation experiment.[12] In this experiment, the slinky pattern in RFX was forced to rotate via the imposition of an externally generated, predominantly 0,1, propagating, magnetic perturbation. The enforced rotation of the slinky pattern lead to a significant diminution of the usual edge loading problems, and, thus, allowed the toroidal plasma current to be raised. Our simulations (as well as the theory outlined in Sec. V) explain some aspects of the RFX mode-rotation experiment: In particular, the behavior of the $m = 1$ phases. However, it is clear that further simulations, which contain more physics (such as multi-harmonic error-fields and vacuum vessel eddy currents), will have to be performed in order to account for all the features of this experiment.

Although our phase evolution equations (and the theoretical ideas which underlie them) are capable of explaining virtually all salient facts regarding the phase-locking of tearing modes in the RFX experiment, there are a number of improvements which we intend to make in the future. First, and foremost, we plan to take finite equilibrium plasma pressure into account in our analysis. This will enable us to employ a more realistic model plasma equilibrium, and will, hopefully, lead to calculated overlap integrals whose sign matches that inferred from experiment. We also hope to incorporate evolution of the relative $m = 0$ phases into our equations—at the moment, $m = 0$ phase-locking is assumed *a priori*. As we have already mentioned, vacuum vessel eddy currents play an important role in the locking of the slinky pattern to static error-fields, as well as in the torque balance equation of a rotating slinky pattern.[14,15] Thus, the incorporation of such eddy currents into our system of equations would represent an important step forward. Finally, we intend to use our equations to model the response of the slinky pattern to multi-harmonic error-fields. In principle, such error-fields can modify the structure of the pattern (there is clear evidence for this in the RFX mode-rotation experiment[12]). Indeed, it is conceivable that a correctly designed multi-harmonic error-field could completely disrupt the slinky pattern.

[1]The conventional definition of this parameter is $q(r) = rB_\phi / R_0 B_\theta$, where r is the radial distance from the magnetic axis, R_0 the plasma major radius, and $\boldsymbol{B} = [0, B_\theta(r), B_\phi(r)]$ the equilibrium magnetic field.

[2]J. B. Taylor, Phys. Rev. Lett. **33**, 1139 (1974).

[3]S. Ortolani and D. D. Schnack, *Magnetohydrodynamics of Plasma Relaxation* (World Scientific, Singapore, 1993).

[4]A. B. Rechester and M. N. Rosenbluth, Phys. Rev. Lett. **40**, 38 (1978).

[5]F. Gnesotto, P. Sonato, W. R. Baker *et al.*, Fusion Eng. Des. **25**, 335 (1995).

[6]T. Tamano, W. D. Bard, C. Chu *et al.*, Phys. Rev. Lett. **59**, 1444 (1987).

[7]A. F. Almagri, S. Assadi, S. C. Prager, J. S. Sarff, and D. W. Kerst, Phys. Fluids B **4**, 4080 (1992).

[8]A. Buffa, F. Gnesotto, V. Antoni *et al.*, in *Proceedings 21st EPS Conference on Controlled Fusion and Plasma Physics, Montpellier, 1994* (European Physical Society, Petit-Lancy, 1994), Vol. 18B, part I, p. 458.

[9]G. Hedin, Plasma Phys. Controlled Fusion **40**, 1529 (1998).

[10]Y. Yagi, H. Koguchi, H. Sakakita *et al.*, Phys. Plasmas **6**, 3824 (1999).

[11]P. Zanca, D. Bettella, S. Martini, and M. Valisa, J. Nucl. Mater. **290–293**, 990 (2001).

[12]R. Bartiromo, T. Bolzonella, A. Buffa *et al.*, Phys. Rev. Lett. **83**, 1779 (1999).

[13]G. Chitarin, A. Masiello, S. Peruzzo, R. Piovan, P. Sonato, and G. Zollino, Plasma Phys. Controlled Fusion **43**, 543 (2001).

[14]R. Fitzpatrick, S. C. Guo, D. J. Den Hartog, and C. C. Hegna, Phys. Plasmas **6**, 3878 (1999).

[15]R. Fitzpatrick and E. P. Yu, Phys. Plasmas **7**, 3610 (2000).

[16]D. D. Schnack and S. Ortolani, Nucl. Fusion **30**, 277 (1990).

[17]K. Kusano, T. Tamano, and T. Sato, Nucl. Fusion **31**, 1923 (1991).

[18]R. Fitzpatrick, Phys. Plasmas **6**, 1168 (1999).

[19]P. Zanca, E. Martines, T. Bolzonella *et al.*, Phys. Plasmas **8**, 516 (2001).

[20]The standard large aspect-ratio ordering is $R_0/a \gg 1$, where R_0 and a are the major and minor radii of the plasma, respectively.

[21]The conventional definition of this parameter is $\beta = 2\mu_0 \langle p \rangle / \langle B^2 \rangle$, where

$\langle \cdots \rangle$ denotes a volume average, p is the plasma pressure, and B is the magnetic-field strength.

[22] W. A. Newcomb, Ann. Phys. (N.Y.) **10**, 232 (1960).

[23] R. Fitzpatrick and E. Rossi, Phys. Plasmas **8**, 2760 (2001).

[24] H. P. Furth, J. Killeen, and M. N. Rosenbluth, Phys. Fluids **6**, 459 (1963).

[25] R. Fitzpatrick, Nucl. Fusion **33**, 1049 (1993).

[26] C. C. Hegna, Phys. Plasmas **3**, 4646 (1996).

[27] A. K. Hansen, A. F. Almagri, D. Craig *et al.*, Phys. Rev. Lett. **85**, 3408 (2000).

[28] P. Fiorentin, G. Marchiori, E. Martines, and P. Sonato, in *Proceedings 20th EPS Conference on Controlled Fusion and Plasma Physics, Lisbon, 1993* (European Physical Society, Petit Lancy, 1993), Vol. 17C, part II, p. 447.

[29] P. Zanca and S. Martini, Plasma Phys. Controlled Fusion **43**, 121 (2001).

[30] P. Zanca and S. Martini, Plasma Phys. Controlled Fusion **41**, 1251 (1999).

[31] Y. Yagi, H. Koguchi, H. Sakakita *et al.*, Phys. Plasmas **8**, 1625 (2001).